Faculdade de Engenharia da Universidade do Porto

Synthesis of Hydroxyapatite and Sericin nanocomposites

Anabela Alves Veiga

Master in Bioengineering

Adviser: Dr. Fernando Rocha (Professor at FEUP and Researcher at LEPABE)
Co-adviser: Dra. Filipa Castro (Post-doctoral researcher at LEPABE)
Dra. Ana Oliveira (Professor at ESB and Researcher at CBQF)

February 2018

Resumo

Os nanocompósitos de hidroxiapatite (HAp) e sericina (SS) representam uma nova classe de biomateriais com propriedades únicas. Por um lado, a hidroxiapatite nanométrica (nano-HAp) é o principal constituinte dos tecidos duros, exibindo propriedades de biocompatibilidade, bioatividade e osteocondutividade. Por outro lado, a SS mostrou melhorar a proliferação celular quando utilizada como matriz orgânica ou como meio para o crescimento celular. Estas características tornam este material um excelente candidato para aplicações biomédicas, nomeadamente para engenharia de tecidos ósseos.

Neste contexto, o objetivo do presente trabalho consistiu na síntese de nanocompósitos de HAp/SS com propriedades controladas (pureza, tamanho, distribuição de tamanho e morfologia) através de uma metodologia simples. Para isso, a precipitação de HAp com diferentes concentrações de SS foi estudada em *batch*, num tanque agitado (ST) e num meso reator de fluxo oscilatório (meso-OFR). O desempenho de ambos os reatores foi comparado através da monitorização do perfil de pH e da caracterização das partículas produzidas. Estas foram avaliadas em termos de pureza e cristalinidade (espectroscopia de infravermelho com transformada de Fourier (FTIR), difração de raios-X (DRX)), distribuição de tamanho (difração a laser), bem como tamanho e morfologia (microscopias eletrónicas de varrimento (SEM), de transmissão (TEM) e de varrimento por transmissão (STEM)).

As nanopartículas de HAp e HAp/SS foram sintetizadas com sucesso em ambos os reatores. Embora as condições hidrodinâmicas dos dois reatores não sejam diretamente comparáveis, os resultados demonstraram um melhor desempenho do meso-OFR quando comparado ao ST, já que o processo de precipitação foi cerca de quatro vezes mais rápido. As partículas obtidas apresentam-se em forma de bastonete e placa, e têm baixa cristalinidade e deficiência em cálcio, características semelhantes à HAp biológica. Os resultados demonstram ainda que a concentração de SS tem influência no tamanho, morfologia, agregação e cristalinidade das partículas de HAp. Na verdade, há um aumento do tamanho médio e um maior número de partículas em forma de placas com aumento da concentração de SS. Para além disso a presença de SS aumenta a agregação das partículas formadas e diminui a sua cristalinidade.

Devido às suas características, estes nanocompósitos representam um biomaterial com potencial para aplicação em regeneração de tecidos ósseos, gerando uma resposta biológica melhorada em termos de diferenciação e proliferação celular e permitindo o estudo do processo de biomineralização.

Abstract

Hydroxyapatite (HAp) and sericin (SS) nanocomposites represent a new class of biomaterials with unique properties. On one hand, nanometric hydroxyapatite (nano-HAp) is the primary constituent of hard tissues, exhibiting properties of biocompatibility, bioactivity and osteonductivity. On the other hand, SS has shown an improvement in cell proliferation when used as an organic matrix or as a medium for cell growth. These characteristics make these materials excellent candidates for biomedical applications, namely for bone tissue engineering.

In this context, the objective of the present work consisted in the synthesis of HAp/SS nanocomposites with controlled properties (purity, size, size distribution and morphology) through a simple methodology. For this, precipitation of HAp with different SS concentrations was studied in batch, in a stirred tank (ST) and in a meso oscillatory flow reactor (meso-OFR). The performance of both reactors was compared by monitoring the pH profile and characterizing the particles produced. These were evaluated in terms of purity and crystallinity (Fourier transform infrared (FTIR), X-ray diffraction (XRD)), size distribution (laser diffraction), as well as size and morphology (scanning electron microscopy (SEM), transmission electron microscopy (TEM) and scanning transmission electron microscopy (STEM)).

Nanoparticles of HAp and HAp/SS were successfully synthesized in both reactors. Although the hydrodynamic conditions of the two reactors were not directly comparable, the results demonstrate the best performance of the meso-OFR when compared to the ST, since the precipitation process was about four times faster. The obtained particles present both rod and plate-like shape, and have low crystallinity and calcium deficiency, characteristics which are similar to biological HAp. The results further demonstrate that the concentration of SS had an influence on the size, morphology, aggregation and crystallinity of HAp particles. In fact, there was an increase in the mean particle size and a larger number of plate-like particles with increasing SS concentration. In addition, the presence of SS increases the aggregation of the formed particles and decreases their crystallinity.

Due to their characteristics, these nanocomposites represent a biomaterial with potential for application in regeneration of bone tissues, generating an improved biological response in terms of cell differentiation and proliferation and allowing the study of the biomineralization process.

Agradecimentos

À Doutora Filipa Castro e ao Professor Fernando Rocha pela motivação, incentivo e disponibilidade durante o decorrer de todo projeto. À Professora Ana Oliveira pela sua contribuição que foi preciosa para a valorização do trabalho. Acima de tudo, estou muito grata por me terem dado esta oportunidade.

A todos os técnicos que me ajudaram nas diferentes técnicas de caracterização.

Às unidades de investigação do LEPABE (FEUP) e do CBQF (ESB).

A todos os investigadores do E-204B, em especial à Antónia, Carolina, Cecília, Ioana e Patrícia, pela boa disposição e companheirismo.

Aos meus amigos, em especial à Marta pela amizade, força e apoio em todos os momentos.

Ao Gustavo, pelo apoio incondicional, paciência e pela atenção sem reservas.

Em especial aos meus pais e ao meu irmão, por tudo.

POCI-01-0145-FEDER-006939 (Laboratory for Process Engineering, Environment, Biotechnology and Energy – UID/EQU/00511/2013) funded by the European Regional Development Fund (ERDF), through COMPETE2020 - Programa Operacional Competitividade e Internacionalização (POCI) and by national funds, through FCT - Fundação para a Cie e a Tecnologia.

NORTE-01-0145-FEDER-000005 – LEPABE-2-ECO-INNOVATION, supported by North Portugal Regional Operational Programme (NORTE 2020), under thencia Portugal 2020 Partnership Agreement, through the European Regional Development Fund (ERDF).

Index

Chapter 1 ..... **1**

Introduction 1
1.1 Contextualization of the work developed 2
1.2 Organization of the dissertation 4

Chapter 2 ..... **5**

Biomaterials 5
2.1 Definition and characteristics 6
2.2 Classes and biological bases for bone application 6
2.3 Calcium phosphates (CaPs) 7
2.3.1 Hydroxyapatite (HAp) 7
Structure 8
Composition 8
Phase Stability 9
Synthesis 10
Mechanical Properties 10
2.4 HAp Composites 11
2.4.1 Sericin (SS) 11
Origin and Importance 11
Silk structure and composition 12
SS extraction 13
Applications 13
2.4.2 HAp/SS Nanocomposites 13

Chapter 3 ..... **15**

Crystallization and Precipitation Processes 15
3.1 Crystallization 16
3.1.1 Supersaturation 16
3.1.2 Nucleation 17
Homogeneous nucleation 17
Heterogeneous nucleation 18
Secondary nucleation 19
3.1.3 Induction time 19
3.1.4 Crystal growth 19
3.1.5 Phase diagram 21
3.2 Precipitation 21
3.2.1 Definition and stages 21
3.2.2 Chemical aspects 23
3.2.3 Physical aspects 23

Chapter 4 ..... **25**

Reactors 25
4.1 Stirred tank reactor 26
4.1.1 Stirred tank batch reactor (ST) 26
4.1.2 Stirred tank semi batch reactor (STS) 26
4.1.3 Continuous stirred tank reactor (CSTR) 26
4.2 Microreactors 27
4.3 Meso oscillatory flow reactor (meso-OFR) 28

Chapter 5 ..... **31**

Materials and Methods 31
5.1 Materials and Reagents 31
5.2 Description of the experimental set-ups 31
5.2.1 ST 31
5.2.2 Meso-OFR 31
5.3 SS extraction 32
5.4 Synthesis of HAp/SS nanocomposites 32
5.5 Sample Characterization 33
pH profile 33
FTIR (Fourier-transform infrared spectroscopy) 34
XRD (X-Ray Diffraction) 34
Laser granulometry 34
SEM, TEM and STEM (Scanning electron, Transmission electron and Scanning Transmission microscopy) 34
5.6 - Comparison of the HAp particles obtained with those of the NETMIX reactor 35

Chapter 6 37

Results and Discussion 37
6.1 pH profile 37
6.2 FTIR 39
6.3 XRD 42
6.4 Particle size distribution 43
6.5 SEM and TEM 45
6.6 - Comparison of the HAp particles obtained with those of the NETMIX reactor 50

Chapter 7 51

Conclusions 51
7.1 Objectives achieved and main conclusions 51
7.2 Limitations and Solutions 52
7.3 Future work and perspectives 53

References 54

Appendices 62
A.1 - Characteristics of interest in a biomaterial [1]. 63
A.2 - Biomedical materials with CaPs [3]. 63
A.3 - Types of bioceramics used in biomedical engineering [144]. 63
B.1 - Ca/P of different CaPs [145],[132]. 64
B.2 - Methods for the synthesis of HAp. 65
C.1 - Degumming methods to extract raw silk proteins. 68
C.2 - SS Applications. 69
D - Published papers on HAp/SS materials. 70
E - pH value and duration of the phases identified for the experimental conditions studied in the ST. 72
F - Experiment performed with 10 times the initial reactants concentration (A) FTIR (B) SEM and (C) TEM. 73

List of figures

Figure 1 - Representative scheme of the different types of biomaterials [17]. 6

Figure 2 – (A) Hexagonal structure; (B) Monoclinic structure. The calcium atoms are vertices of the triangles that are surrounding the hydroxyl groups [31],[40]. 8

Figure 3 - Solubility isotherms of CaPs at 37 °C, where the solubility isotherms are expressed in Log [Ca] as a function of pH [39]. 9

Figure 4 - Hierarchical structure of bone from a macro to a nanoscale [45]. 11

Figure 5 - Types of Nucleation [74]. 17

Figure 6 - Variation of ΔG with r and behavior of an embryo according to its size [37],[31]. . 18

Figure 7 - Contact angle and interfacial tension [37]. 19

Figure 8 - A- Kossel's model of a growing crystal surface (A-flat surfaces; B-steps; C-Kinks; D- surface-adsorbed growth units; E-edge vacancies; F-surface vacancies) [37], [73]. .. 20

Figure 9 - Schematic representation of the processes involved in the crystal growth (1) Transport of solute to a position near the crystal surface; (2) diffusion through boundary layer; (3) adsorption onto crystal surface; (4) diffusion over the surface; (4*) desorption from the surface; (5) attachment to a step or edge; (6) diffusion along the step or edge; (7) Incorporation into kink site or step vacancy [76]. 20

Figure 10 - Phase diagram [31]. 21

Figure 11 - Schematic representation of the A-aggregation and B-agglomeration phenomena [74]. 22

Figure 12 - Ostwald ripening effect [37]. 23

Figure 13 - A) ST; B) STS, where v(t) is the flow rate that can vary over time; C) CSTR (Volume V, at temperature T, is the same throughout the reactor and at any time. Fi^{*0} is the molar flow rate of species i^* in the reactor, while Fi^* is the molar flow rate of species i^* outside the reactor [84]. 27

Figure 14 – Flow regimes (A) turbulent flow; (B) laminar flow [93]. 28

Figure 15 - Schematic representation of cross section in an OFR [95]. 28

Figure 16 - Mechanism of oscillatory flow mixing (OFM) in an OFR [97]. 29

Figure 17 - Geometry of the meso-OFR [20]. 29

Figure 18 - Experimental set-ups for the precipitation of HAp/SS nanocomposites (A) ST (B) meso-OFR. 32

Figure 19 - Representative scheme of the SS extraction process in boiling water. 32

Figure 20 - Flowchart of the method for the preparation of HAp/SS nanocomposites. 33

Figure 21 – Variation of pH over time for the experimental conditions studied in the ST for the entire experimental time (A) and for the first 500 s (B). 37

Figure 22 - Stages identified in the ST pH profiles for (A) HAp (B) HAp/SS1 and (C) HAp/SS2. 38

Figure 23 - Variation of pH over time for the experimental conditions studied in the meso-OFR for the entire experimental time (A) and for the first 2500 s (B). 38

Figure 24 - FTIR spectra of the particles produced in the ST. 39

Figure 25 - FTIR spectra of the particles produced in the meso-OFR. 40

Figure 26 – XRD patterns of the particles produced in the ST. 42

Figure 27 - Particle size distribution in number of the particles produced in the ST (A) and the meso-OFR (B)..... 44

Figure 28 - Particle size distribution in volume of the particles produced in the ST (A) and the meso-OFR (B)..... 44

Figure 29 – (A) SEM (B) TEM images of the commercial HAp. 45

Figure 30 – (A) SEM, (B) TEM and (C) STEM images of the HAp particles obtained in the ST. .. 47

Figure 31 - (A1) HAp/SS1 SEM; (B1) HAp/SS1 TEM; (A2) HAp/SS2 SEM; (B2) HAp/SS2 TEM images of HAp/SS particles obtained in the ST. 47

Figure 32 - (A) SEM and (B) TEM images of HAp particles obtained in the meso-OFR. 48

Figure 33 – (A) SEM and (B) STEM images of HAp/SS1 particles obtained in the meso-OFR. ... 48

Figure 34 – (A) SEM and (B) STEM images of HAp/SS2 particles obtained in the meso-OFR. ... 48

Figure 35 - EDS of the samples obtained in the ST (A) HAp (B) HAp/SS1 and (C) HAp/SS2. 49

Figure 36 - EDS of the samples obtained in the meso-OFR (A) HAp; (B) HAp/SS1; (B) HAp/SS2. 49

List of tables

Table 1 - Bone formation mechanisms [17]. 7

Table 2 - Solubility at 37 ºC of different CaPs [41]. 10

Table 3 - Mechanical Properties of HAp and human bone tissues. 11

Table 4 - SS properties [55],[60],[64]. 12

Table 5 - Differences between crystallization and precipitation [5]. 22

Table 6 – Different types of reactors used to obtain HAp. 27

Table 7 - Operating Conditions studied. 33

Table 8 - Identification of the functional groups present in the FTIR spectra of the samples obtained in the ST and the meso-OFR [100],[66]. 41

Table 9 - Identification of the peaks present in the XRD patterns of the samples obtained in the ST. 43

Table 10 - Parameters of the particle size distribution in number of the powders produced in the ST and the meso-OFR at different operating conditions. 45

Table 11 - Characteristics of the obtained particles and the particles obtained in the NETMIX reactor [83],[91],[106]. 50

Table 12 - Summary of the main conclusions of the work developed. 53

Abbreviations and symbols

Notation

a_i - Activity of a supersaturated solution, M (equation 1.2)
$a^*{}_i$ - Activity of a saturated solution, M (equation 1.3)
A - Pre-exponential factor, $m.kg^g.s^{-1}.g^{-g}$ (equation 1.17 and 1.18)
C - Concentration of the solute in solution, ($g.kg^{-1}$) (M) (equation 1.5, 1.6 and 1.7)
C^* - Equilibrium concentration, ($g.kg^{-1}$) (M) (equation 1.5, 1.6 and 1.7)
Ca/P - Molar ratio between calcium and phosphorus atoms
ΔC - Concentration driving force, $g.kg^{-1}$ (equation 1.5)
d_{10} – Size corresponding to the 10th percentile of the size distribution, µm
d_{50} – Size corresponding to the 50th percentile of the size distribution, µm
d_{90} - Size corresponding to the 90th percentile of the size distribution, µm
D – Diameter of the reactor, m (equation 2.1)
E_g - Activation energy of crystal growth, $J.mol^{-1}$ (equation 1.17 and 1.18)
f – Oscillation frequency, Hz
f – Stirring speed, rpm
f_c - Geometric correlation factor (equation 1.13 and 1.14)
F_{i*}^0 - Molar flow rate of species i in the reactor, $mol.s^{-1}$ (Figure 14)
F_{i*} - Molar flow rate of species i outside the reactor, $mol.s^{-1}$ (Figure 14)
g - Order of the overall growth process (equation 1.16)
G - Crystal growth rate, $m.s^{-1}$ (equation 1.16)
ΔG - Free energy of Gibbs, J (equation 1.9, 1.10 and 1.11)
ΔG_s - Free energy variation for the formation of the core surface, J (equation 1.9)
ΔG_v - Free energy change of the transformation per unit volume, $J.m^{-2}$ (equation 1.10)
ΔG_V - Variation of free energy for phase transformation, J (equation 1.9, 1.10 and 1.11)
ΔG_{crit} - Activation energy, J
$\Delta G_{c,het}$ - ΔG of the critical nucleus formed by heterogeneous nucleation, J (equation 1.13)
$G_{c,hom}$ - ΔG of critical nuclei in the homogeneous process, J (equation 1.14)
i – Solute
J - Rate of nuclei formation, $s^{-1}.L^{-1}$ (equation 1.12)
k_g - Growth rate constant, $m.kg^g.s^{-1}.g^{-g}$ (equation 1.16 and 1.17)
K - Boltzmann constant, $1.38064852 \times 10^{-23}$ $m^2.kg.s^{-2}.K^{-1}$
Ksp - Solubility product constant (Table 2)
r - Size of the cluster, m (equation 1.10 and 1.11)
r_c - Critical size of the nucleus, m (equation 1.11)
R - Gas constant, 3.3143 $mol^{-1}.K^{-1}$
Re - Reynolds number (equation 2.1)
Re_0 - Oscillatory Reynolds number (equation 2.2)
S - Supersaturation ratio (equation 1.6 and 1.7)
St - Strouhal number (equation 2.3)

t_g - Time that elapses until the crystals become visible, s (equation 1.16)
t_{ind} – Induction time, s (equation 1.16)
t_n – Time that elapses until the formation of stable nucleus, s (equation 1.16)
t_r - Relaxation time, s (equation 1.16)
T - Absolute temperature, K
V - Flow velocity, $m.s^{-1}$ (equation 2.1)
x_i - Molar fraction in the solution (equation 1.2 and 1.3)
x_0 - Oscillation amplitude center-to-peak, m

List of greek symbols

ρ - Fluid density, $kg.m^{-3}$ (equation 2.1)
σ - Relative supersaturation (equation 1.7)
θ - Contact angle between liquid and solid surface (equation 1.14 and 1.15)
μ - Dynamic viscosity, $kg.m^{-1}.s^{-1}$ (equation 2.1)
$\Delta\mu$ – Driving force for crystallization, $J.mol^{-1}$ (equation 1.1)
μ_i - Supersaturated solution, $J.mol^{-1}$ (equation 1.1, 1.2 and 1.4)
μ_i^* - Saturated solution, $J.mol^{-1}$ (equation 1.1, 1.3 and 1.4)
μ_i^0 - Standard chemical potential of specie i, $J.mol^{-1}$
γ - Surface tension, $J.m^{-2}$
γ_{sl} - Solid-liquid interfacial tension (equation 1.15)
γ_{cs} - Crystal-solid interfacial tension (equation 1.15)
γ_{cl} - Crystal-liquid interfacial tension (equation 1.15)
Υ_i - Activity coefficient
w- Angular frequency of oscillation, s^{-1}

Acronyms

ACP - Amorphous calcium phosphate
APPACDM - Associação Portuguesa de Pais e Amigos do Cidadão Deficiente Mental de Castelo Branco
CaPs - Calcium phosphates
CBQF - Centre for Biotechnology and Fine Chemistry
CEB - Centre of Biological Engineering
CPP - Calcium pyrophosphate
CPPD - Calcium pyrophosphate dihydrate
CSTR - Continuous stirred tank reactor
$CaCl_2.2H_2O$ - Calcium chloride dihydrate
DEB - Center of Biological Engineering
DCP - Dicalcium phosphate dehydrate
DCPD - Dicalcium phosphate dehydrate
EDS - Energy-dispersive X-ray spectroscopy
ESB - Faculty of Biotechnology of the Catholic University of Portugal
FEUP - Faculty of Engineering of the University of Porto
FTIR - Fourier transform infrared
HAp – Hydroxyapatite

HAp/SS1 – Hydroxyapatite with 0,1 $g.L^{-1}$ of SS
HAp/SS2 - Hydroxyapatite with 1 $g.L^{-1}$ of SS
HCP - Calcium heptaphosphate
LEPABE - Laboratory of Process Engineering, Environment, Biotechnology and Energy
MCPM - Monocalcium phosphate monohydrate
Meso-OFR - meso oscillatory flow reactor
Nano – Nanometric
Na_2HPO_4 - Disodium hydrogen phosphate
OCP – Octacalcium phosphate
OFR - Oscillatory flow reactor
OFM - Oscillatory flow mixing
OHAp - Calcium deficient HAp
PCL - Polycaprolactone
PGA - Polyglycolic acid
PLGA - Polylactic-coglycolic acid
PLLA - Poly L-lactic acid
Rpm – Rotation per minute
SAED - Selected area electron diffraction
SEM - Scanning electron microscopy
SPC- Smooth periodic cavities
SS - Sericin
ST - Stirred tank batch reactor
STS - Stirred tank semi batch reactor
STEM - Scanning transmission electron microscopy
TEM – Transmission electron microscopy
XRD - X-ray diffraction
(α, α´, β, ϒ) TCP - Tricalcium phosphate

Chapter 1

Introduction

This chapter focuses on the importance of the formation of new biomaterials for bone tissue applications as an alternative to conventional approaches, highlighting hydroxyapatite/sericin (HAp/SS) nanocomposites. The advantages of the use of this type of materials, as well as their characteristics are presented. The synthesis method of the nanocomposites (precipitation), and the reactors used in the experimental activities (stirred tank batch reactor (ST) and meso oscillatory flow reactor (meso-OFR)) are clarified. This introduction aims at identifying the scientific, technological and economic interests of the studied subject and the motivation of the work developed. Finally, it is established the organization and contents addressed in each chapter of this dissertation.

1.1 Contextualization of the work developed

For several decades, repair and regeneration of bone tissue has been a complicated and common clinical problem for different generations. The Gold Standard bone repair technique, known as transplantation, includes the use of bone grafts to stimulate bone growth at the implant site. Graft is a piece of tissue that is transferred from a donor site to a recipient site in order to reconstruct it, either from the patient itself (autologous), from a human donor (allogenic) or obtained from donors of other species (xenogenic) [1]. The transplantation presents disadvantages such as the difficulty in obtaining enough bone graft to fill all the bone defect. In addition, it is an invasive technique that can involve risks. Autologous and xenogenic grafts, although reducing surgical risks and being able to be obtained from virtually inexhaustible sources, may lead to the transmission of diseases and/or provoke immunological reactions [2].

With the evolution of science there has been an increase in the number of promising alternatives for the treatment of bone defects, namely biomaterials that promote bone regeneration. HAp is one of the most used materials for this purpose due to its excellent biocompatibility and osteoconductive properties, and similarity to the inorganic part of human bones and teeth [3]. However, the use of HAp has limitations due to its low toughness and poor mechanical resistance under complex stress states, characteristic of most ceramics, which increases the risk of fracture and limits the clinical applications of this material. Thereby, the preparation of HAp composites for bone regeneration has several advantages, namely the possibility of improving HAp properties, such as mechanical strength and biological response [4],[5].

The organic matrix has been reported to play an important role during the formation of biominerals (biomineralization), since it controls the location and organization of nucleation sites, as well as the structure and orientation of the HAp crystals. But the mechanism of HAp formation has not yet been fully understood [6].

Therefore, further investigations on HAp/organic composite materials is necessary for both the development of applicable bone implant materials and for understanding of crystallization during the process of biomineralization [4].

Many studies on composites combining synthetic HAp particles with other materials have been conducted. These materials include synthetic polymers (polyglycolic acid (PGA), poly L-lactic acid (PLLA), polylactic-coglycolic acid (PLGA) and polycaprolactone (PCL)) [7], natural polymers (alginate, chitosan, cellulose) [8], proteins (collagen and fibroin) [9] or combinations of the foregoing [10]. Synthetic polymers may induce local and systemic host reactions due to the release of chemicals and monomers from polymer degradation, while natural polymers may lead to products with different characteristics due to the differences in raw materials. The majority of the studies carried out focus on the use of collagen, since it is a main component of bones. However, clinical application of collagen-type implants is still limited because of its drawbacks such as its high cost, increased risk of cross-infections, weak mechanical properties and fast degradability [4],[11].

Special attention has been given to nanometric-HAp (nano-HAp), because of its similarity in size, crystallinity and chemical composition with bone. Nano-HAp has special properties due to its nanometric scale, chemical composition, shape and surface. Due to its high surface to volume ratio, nano-HAp is more efficient and reactive as compared to other materials of higher

dimensions, leading to unique properties for bone repair [12]. These characteristics and its bioactive and biosorbent nature, make it a suitable material for bone tissue engineering [13].

Silk sericin, the soluble protein from the cocoon of the *Bombyx Mori* silkworm, represents about 50,000 tons of all raw silk thread processing (100 kg of silk produces almost 22 kg of SS), and was traditionally disposed in silk processing wastewater [14]. Recently there has been a growing interest in its recovery due to its beneficial properties, as well as the serious environmental pollution caused by its elimination. The antioxidant potential and the presence of highly hydrophilic amino acids such as serine, which has large capacity to absorb water, are among the properties of interest of SS. These characteristics are widely applied in food, cosmetic and medical industry. The moisturizing capability justifies its use as a therapeutic agent for wound healing, stimulating cell proliferation, and creams for skin hydration and protection against ultraviolet radiation. The antioxidant activity associated with the low digestibility of SS, makes it suitable for biomedical applications, such as antitumor, antimicrobial and anti-inflammatory agent [15]. Moreover, SS has shown an improvement in cell proliferation when used as an organic matrix or as a medium for cell growth [16],[15]. Its combination with HAp particles may thus promote the mechanisms of bone formation. In particular HAp/SS nanocomposites are capable of offering microporous characteristics with high surface area, which is particularly relevant in bone substitution applications [17].

The reported approaches used to obtain HAp/organic nanocomposites are based on alternate soaking, mechanical mixing and precipitation, being the last the simplest route for the synthesis of nano-HAp [11]. This technique is widely used because of its simplicity, cheap raw materials, minimal operation costs and easy application in industrial scale [5]. A common problem of this method is the difficulty in distributing the particles homogeneously at micro scale, thus affecting the crystal size distribution and chemical purity of the precipitated particles [18],[19]. The meso-OFR is a mesoscale (milliliter) device with smooth periodic constrictions, developed by members of the present research team [20]. The basic concept of this reactor is the application of periodic fluid oscillations to a cylindrical column containing evenly spaced orifice baffles. The intensity of the oscillatory flow mixing is controlled by the oscillation frequency (f) and amplitude (x_o). The meso-OFR has demonstrated a significant enhancement in processes such as mass transfer and particle mixing in multiphase systems [21], making it a good candidate to promote ideal conditions for the controllability of HAp particles properties. Moreover, meso-OFR reduces reagent requirements and waste. This reactor offers thus advantages in terms of costs [19].

In the present work, synthesis of HAp/SS nanocomposites was achieved through a batch precipitation process in a stirred tank batch reactor (ST) and a meso-OFR. The inclusion of SS aims at enhancing HAp mechanical strength and biological response, making it more suitable for bone tissue engineering. Different concentrations of SS were studied and the pH profile was monitored for each experimental condition. The performance of both reactors was then compared by characterizing the resulting HAp/SS composites in terms of purity and crystallinity (Fourier transform infrared (FTIR) spectroscopy, X-ray diffraction (XRD)), size distribution (laser granulometry), size and morphology (scanning electron microscopy (SEM), transmission electron microscopy (TEM) and scanning transmission electron microscopy (STEM)), and by analyzing the obtained pH profiles.

1.2 Organization of the dissertation

This dissertation is organized in 7 chapters described below. From chapter 1 to chapter 5 the state of the art and the theoretical foundations of the topics addressed, as well as the methodology and equipment used to obtain the HAp/SS nanocomposites are covered. In chapter 6, the results are presented and discussed. Finally, chapter 7 presents the main conclusions of this dissertation and suggestions for future work.

- Chapter 1 – Introduction - Description and framework of the project developed, summarizing the concepts of interest of the present dissertation;
- Chapter 2 - Biomaterials - Presentation of the biomaterials used in bone tissue engineering, namely HAp and SS;
- Chapter 3 - Crystallization and Precipitation Processes - Theoretical concepts related to crystallization and precipitation processes, namely mechanisms, and physical and chemical aspects of precipitation.
- Chapter 4 - Reactors - Description of the reactors that have been used for the precipitation of HAp;
- Chapter 5 - Materials and Methods - Description of the experimental procedure, materials and equipment used to obtain HAp/SS nanocomposites;
- Chapter 6 - Results and Discussion - Presentation and discussion of the experimental results obtained;
- Chapter 7 - Conclusions - General conclusions, goals met, limitations encountered and future perspectives.

Chapter 2

Biomaterials

In this chapter, the basic concepts of biomaterials, such as definition, characteristics and classes, are reviewed. Bioceramics such as calcium phosphates (CaPs) are addressed, emphasizing HAp and its nanocomposites. The use of nanometric HAp is justified, clarifying its unique properties. This section aims at highlighting the characteristics and advantages of the conjugation of HAp with SS for the formation of nanocomposites for bone application.

Concerning HAp, several aspects are discussed such as its structure, phase stability, different synthesis methods (such as wet methods) and its mechanical properties. As for SS, its origin, extraction methods (such as extraction of SS in boiling water) and health care applications are addressed. The use of the chemical precipitation method to obtain the nanocomposites developed in this work, and the extraction of SS by heat, is fundamentally due to its simplicity, ready availability and minimal operation costs.

2.1 Definition and characteristics

Biomaterials are substances or a combination of two or more substances of a synthetic or natural origin, which may be used for a period of time, to partially or wholly improve or enlarge tissues or organs in biological systems [22]. There are several characteristics a biomaterial should have, according to its purpose and application, such as biocompatibility, mechanical properties and size suitable for use, among others (Appendix A.1). Biocompatibility refers to materials that are compatible with living tissue or system by not being toxic, injurious, or physiologically reactive and not causing immunological rejection [1].

Biomaterials are used in Biomedical Engineering for many purposes such as, cardiovascular medical devices, ophthalmologic applications, bioelectrodes and biosensors, burn dressings and skin substitutes, sutures, drug delivery systems and orthopedic and dental applications [23]. Several biomaterials have been used in bone tissue engineering, especially bioceramics such as CaPs (Appendix A.2) [3].

The performance of biomaterials *in vivo* can be classified in different ways. The natural biomaterials include protein (fibroin, sericin, fibrin, elastin, collagen and keratin) and polysaccharide (alginate, amylose, chitin, cellulose, chitosan and agarose) origin materials, while the synthetic include metallic, polymeric, ceramic and composite materials, being the last two of interest in the present work (Figure 1) [17-[24].

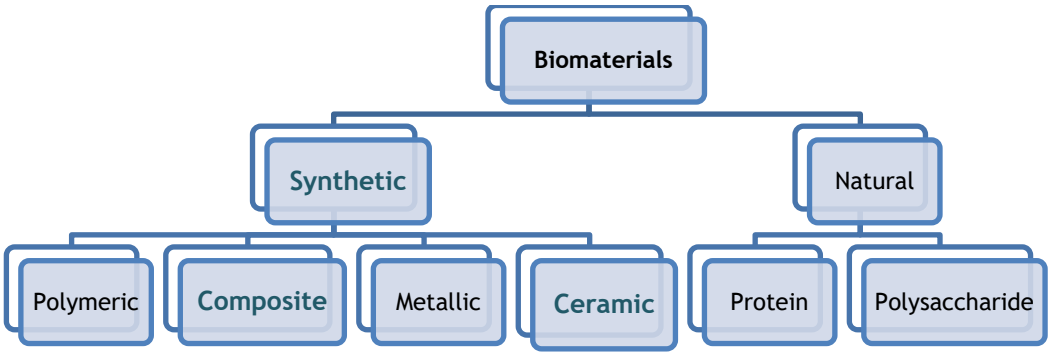

Figure 1 - Representative scheme of the different types of biomaterials [17].

Biomaterials can also be classified according to their biological behavior based on host tissue response. Biomaterials can be bioinert, bioactive, biotolerant and biodegradable. Bioinert retain their physical and mechanical properties over the lifetime of the clinical implant. These materials have minimal biochemical reactivity with the host tissue, being considered stable. Bioactive biomaterials establish chemical bonds with the living tissue that promote cell growth and do not produce toxic or harmful reactions. Biodegradable or resorbable materials can be chemically degraded or decomposed by natural effectors, and converted into new tissue [25]. Biotolerant materials are those that are not rejected when implanted into the living tissue but are surrounded by layers of fibrous tissue. Metals and polymers are usually considered biotolerant materials and are mainly used due to their mechanical properties of sustentation [26].

2.2 Classes and biological bases for bone application

Ceramics are commonly bioactive, bioinert or biodegradable materials [5]. This class of materials is usually formed by metallic and nonmetallic elements bonded by ionic and/or covalent bonds. In these bonds, the electrons are not free as they occur in metals but are

located between the ions. Ceramics tend to behave as hard and brittle materials with high compressive strength, being highly inert and good electrical and thermal insulators [17]. The class of ceramics used to repair, regenerate or replace damaged parts of the musculo-skeletal system are referred to as bioceramics (Appendix A.3) [27]. Bioceramics are highly used in hard tissue repair, such as bone and teeth [28].

Among ceramics, CaPs based materials are widely used in bone tissue engineering. These bioceramics have a similar composition with the inorganic component of hard tissue, presenting high biocompatibility and bioactivity [29]. There are other characteristics that can describe CaPs used in bone applications, such as osteogenesis, osteoinduction and osteoconduction. These processes represent the bases and biological mechanisms for bone application (Table 1) [26].

Table 1 - Bone formation mechanisms [17].

Osteogenesis	•The process by which living and remaining bone cells in the material maintain the ability to form bone matrix.
Osteoinduction	•Ability to induce the undifferentiated mesenchymal cell, present in the receptor area, to transform into a cell that produces bone (osteoblast).
Osteoconduction	•Ability of a material to serve as a framework on which bone cells can attach, grow and divide. In this way, the bone healing response is "conducted" through the biomaterial site.

2.3 Calcium phosphates (CaPs)

CaPs have three main chemical elements: calcium (oxidation number +2), phosphorus (oxidation number +5) and oxygen (oxidation number -2) and exist in different forms and phases depending on temperature, partial water pressure and the presence of impurities, and can be classified by the molar ratio between calcium and phosphorus atoms (Ca/P) [30],[31]. The free calcium and phosphorus ions in their chemical composition promotes a physical-chemical bond with the bone tissue surrounding. They also allow for bone remodeling at the implant site because of its high *in vivo* degradation time [12].

CaPs apatites generally have the formula $Ca_5(PO_4)_3X$, where X is an electronegative element as a halogen or a hydroxyl group. CaPs with biological importance include amorphous calcium phosphate (ACP), dicalcium phosphate dihydrate or brushite (DCPD), monetite (DCPD), octocalcium phosphate (OCP), tricalcium phosphate (β-TCP), calcium pyrophosphate dihydrate (CPPD) and HAp (Appendix B.1) [30],[17].

The number of articles, patents and designs concerning CaPs with different forms and applications increases annually, among which HAp has received special attention [30].

2.3.1 Hydroxyapatite (HAp)

The present HAp studies have aimed at obtaining biomaterials that meet the biomechanical requirements for an implant, while being compatible with the surrounding biochemical and cellular environment [32]. HAp has biocompatibility and bioactivity properties with respect to bone cells and tissues due to its similarity with the hard tissues of the body [33], being ideal for orthopedic and dental applications, to repair, substitute or regenerate hard tissues [34].

Synthesis of nano-HAp has particular importance due to its similarity in size, crystallinity, and chemical composition with bone [33]. Nano-HAp has a high surface area to volume ratio, being much more efficient and reactive as compared to other materials of higher dimensions, which is particularly relevant for bone tissue engineering [35]. Nano-HAp promotes osteoblast adhesion and proliferation, and the deposition of minerals on the surface of these materials [30]. The stated characteristics coupled with the long residence time of nano-HAp, make it a suitable material for bone tissue engineering [30].

Differences in structure, chemistry and composition of HAp arise from differences in processing parameters such as: time, temperature and atmosphere [36].

Structure

The physical structure of the particles depends on the structural arrangement of their atoms, ions, or molecules. The crystalline structures are characterized by having an ordered grouping of their elements, where it is possible to identify a set of repeating atomic points or positions, known as the unit cell that can be represented by a parallelepiped. Through the adoption of specific lattice parameters, it is possible to characterize a specific crystalline structure. These parameters include the length of the three edges of the parallelepiped (a,b,c) and the three angles between the edges (α, β e γ). HAp acquires a hexagonal ($a = b \neq c$; $\alpha = \beta = 90^\circ$, $\gamma = 120^\circ$) or monoclinic structure ($a \neq b \neq c$; $\alpha = \gamma = 90^\circ$, $\beta \neq 90^\circ$) [37]. The monoclinic structure is thermodynamically more stable, even at room temperature, and corresponds to the stoichiometric HAp, while the hexagonal structure is the most frequently encountered and is characteristic of nonstoichiometric HAp [38].

The HAp unit cell has six PO_4 groups and two OH groups. The calcium and hydroxyl groups are in parallel channels. Through these channels, ion substitution can easily occur, which is characteristic of non-stoichiometric HAp [30],[39]. The structure of HAp allows isomorphic cationic and anionic substitutions with great ease. Ca^{2+} can be replaced by metals such as Pb^{2+}, Cd^{2+}, Cu^{2+}, Zn^{2+}, Sr^{2+}, Co^{2+}, Fe^{2+}, the phosphate groups by carbonates and vanadates, and the hydroxyl groups by carbonates, F^- and Cl^- [18].

The hexagonal form presents a spacing of the $P6_3/m$ space group (characterized by an axis C of 6 units perpendicular to 3 equivalent axes maintaining a triangle of 120º) with lattice parameters a = b = 9.4176 Å and c = 6.8814 Å , $\beta = 120^\circ$ (Figure 2 A). The monoclinic structure presents a spacing of the $P2_1/b$ space group with lattice parameters a = 9.4214 Å, b = 2a, c = 6.8814 Å, $\gamma = 120^\circ$ (Figure 2 B) [39]. The main difference between these two HAp structures is the orientations of the hydroxyl groups. While in monoclinic structure OH ions in each column are pointed in the same direction, and the direction reverses in the next column, in the hexagonal structure adjacent OH ions point in the opposite direction [38]

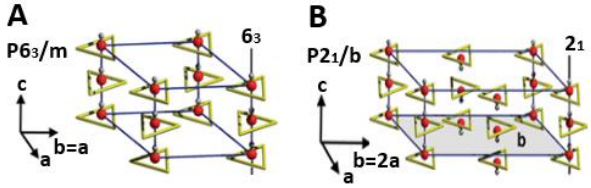

Figure 2 - (A) Hexagonal structure; (B) Monoclinic structure. The calcium atoms are vertices of the triangles that are surrounding the hydroxyl groups [31],[40].

Composition

HAp is the most similar CaP to the mineral constituent of hard tissues, which represents approximately 70% of the mass of vertebrate bones and teeth [34]. This biomaterial has variable composition since it can adopt different chemical compositions ($Ca_{10-x}(PO_4)_{6-x}(HPO_4)_x(OH)_{2-x}$,

where x is between 0 and 1), from stoichiometric HAp ($Ca_{10}(PO_4)_6(OH)_2$) to fully calcium-deficient HAp ($\sim Ca_9HPO_4(PO_4)_5OH$) (OHAp) [41]. The variable Ca/P molar ratio of OHAp can be due to undetected phases, surface adsorption, lattice substitutions, and crystalline mixtures [39].

Biological apatites are usually nanostructured OHAp crystals with Ca/P of less than 1.67, CO_3^{2-} groups and traces of different ions such as HPO_4^{2-} ,Na^+,Mg^{2+}, Sr^{2+},K^+,Cl^- and F^- built into its structure [42],[43]. The incorporation of the CO_3^{2-} ions in the hexagonal channel of the apatite structure, through the substitution of OH^- ions, forms A-type carbonate HAp, while B-type substitution occurs when CO_3^{2-} substitutes primarily for PO_4^{3-} groups. The bone mineral apatite is generally considered to be the B-type [44].

Phase Stability

One of the most important properties of CaPs that influences their performance *in vivo* is their solubility. In order to understand the stability of CaPs in aqueous solutions, it is important to know their solubility under the studied operating conditions [39].

According to the solubility diagram (Figure 3), for any given pH value, any CaP whose isotherm is below the isotherm of another calcium phosphate is less soluble and therefore more stable. With the increase in Ca/P comes the decrease in solubility. It is also possible to verify that in neutral and acidic regions, the slope of the solubility isotherms is negative. This reflects the fact that all compounds are more soluble as the pH decreases. In the alkaline region, calcium concentration increases with increasing pH (Figure 3) [39].

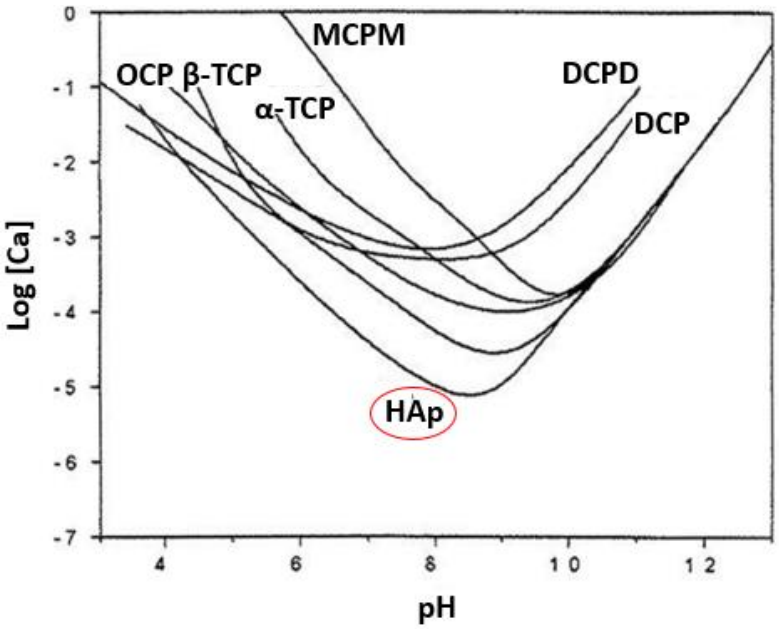

Figure 3 - Solubility isotherms of CaPs at 37 °C, where the solubility isotherms are expressed in Log [Ca] as a function of pH [39].

Under physiological conditions of temperature (37ºC) and pH (6-8), the solubility of CaPs and, consequently, their degradation *in vivo*, is given by the following order: MCPM> α-TCP> DCPD> DCP> OCP> β-TCP> HAp (Figure 3 and Table 2) [39]. Thus, from a thermodynamic point of view HAp is the most stable (less soluble) CaP under physiological conditions of temperature and pH (Figure 3) [30]. However, kinetic factors must also be considered in determining the probability of formation of the different phases of CaPs in supersaturated solutions. The

formation of HAp is slower than that of OCP or that of DCPD, i.e., during the precipitation of CaPs the formation of the kinetically most favored phase can be observed even though it has a lower thermodynamic conduction force. Therefore, it is important to consider kinetic and thermodynamic factors to determine the probability of formation of precursor phases in the precipitation of a CaP [31].

Table 2 - Solubility at 37 ºC of different CaPs [41].

Chemical formula CaPs	Ca/P	Solubility at 37ºC -log (K_{sp})
DCPD	1,00	6,73
OCP	1,33	98,6
ACP	1,5 (1,20-2,20)	Cannot be measured precisely
α-TCP	1,50	28,5
β-TCP	1,50	29,6
HAp	1,67	117,2

Synthesis

HAp can be synthesized in the laboratory by dry methods, wet methods and high temperature processes (Appendix B.2). Depending on the process used, the HAp obtained can have different physicochemical characteristics [5]. Dry methods do not use a solvent and do not require precisely controlled conditions. The particles obtained have large size distribution, irregular shape and high crystallinity. On the other hand, in wet methods the particles obtained have a nanosized structure with regular morphology. This method allows the control of the reaction parameters. However, the low temperatures used, compared to dry methods, can lead to the formation of other CaPs and to the incorporation of ions present in the aqueous solution in the crystal structure. High temperature processes use high temperatures to burn or partially burn the precursors. These methods can avoid the formation of undesirable CaPs phases, generating single phase HAp with high crystallinity. The main disadvantage is that the reaction temperature can be affected by the nature of the fuel or the quantity of the initial precursors therefore producing different HAp products [45].

According to the literature, the conventional wet chemical precipitation method is one of the most widespread approaches for the synthesis of nanosized HAp. This is due to its simplicity, ready availability, cheap raw materials, low reaction temperatures, minimal operation costs and easy application in industrial scale [5].

Mechanical Properties

Despite its properties of interest, the use of HAp has limitations to circumvent such poor mechanical resistance under complex stress states, which increases the risk of fracture. The tensile strength and the fracture toughness of HAp is lower when compared to bone tissue (Table 3). Due to its high fragility, its use is limited in areas where mechanical effort is required [16].

Table 3 - Mechanical Properties of HAp and human bone tissues.

Materials	Properties				
	Density (g/cm^3)	Compressive strength (MPa)	Young's modulus (GPa)	Tensile strength (MPa)	Fracture toughness ($MPa.\ m^{-1/2}$)
HAp	3,16 [35]	300-900 [46]	80-120 [46],[47]	≈40 [48]	0,6-1 [47]
Human bone (cortical)	1,40 [49]	88-230 [46] or 130-180 [48]	3-30 [46] or 12-18 [48]	50-151 [48]	2-12 [47] or 6-8 [48]
Human tooth (dentin)	2,00 [49]	300-380 [46]	15-20 [46]	≈34-62 [50]	≈2,2-3,4 [51]
Human tooth (enamel)	3,00 [49]	250-550[46]	10-90 [46]	≈12-42 [50]	≈0,7-1,4 [52]

One approach that aims to overcome these problems is the combination of this bioceramic with other materials to improve its properties [25]

2.4 HAp Composites

A composite material consists of the union of two or more materials of different natures and properties, which leads to the obtainment of a new material, whose set of properties is better than the properties of the components separately [53]. Bone itself is a composite material, which consists of an organic (collagen) and inorganic (HAp) component, with a hierarchical structure that ranges from the nanoscale to the macro-scale (Figure 4). Other natural composites include wood, dentin, cartilage, and skin [22].

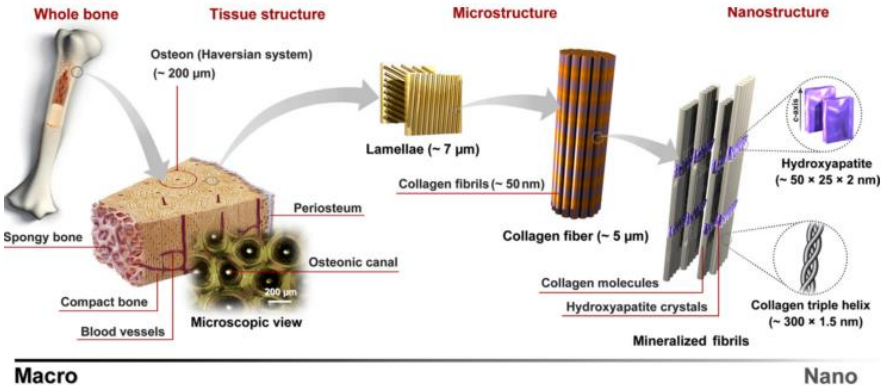

Figure 4 - Hierarchical structure of bone from a macro to a nanoscale [45].

Since HAp is the major mineral constituent of vertebrate bone and tooth [45], as previously referred, and SS can accelerate cell proliferation and attachment [54], HAp/SS conjugates are biomaterials with potential for the treatment of bone defects [40]. HAp/SS composites have shown to have a more controlled degradation and longer residence time *in vivo*, and therefore are suitable for *in vivo* applications [16]. Furthermore, SS has been used for other biomedical applications because of its wound healing properties, its antioxidant and antimicrobial activity, and due to its gelling nature [16].

2.4.1 Sericin (SS)

Origin and Importance

There are several species of insects that produce natural silk, such as spiders and silkworms. The silkworm is a native insect from North China, and currently the most used in the production

of silk threads. Its distribution is very wide, being present in several farms of production known as Sericulture [55]. The most common species of domesticated silkworm is *Bombyx mori*, which has been a major molecular genetic resource for solving a wide range of biological problems in food, textile, pharmaceutical, environmental and biomedical industries [56]. SS represents about 50,000 tons of all raw silk thread processing and was traditionally disposed in silk processing wastewater (100 kg of silk produces almost 22 kg of SS) [57]. In recent years there has been a growing interest in its recovery due to its beneficial properties as well as the serious environmental pollution caused by its elimination. The use of SS recovered from silk industry processes adds value to this protein. If this protein is recovered and recycled it can represent a significant economic, ecologic and social benefit [58],[57].

Silk structure and composition

Silk is a continuous thread mainly consisting of a double layer of fibroin (structural center), coated by SS (material surrounding the structural center) [59],[60]. Moreover, fibroin is a semicrystalline fibrillar protein that provides stiffness and resistance, while SS is an amorphous protein that operates as a binder to maintain structural integrity of the cocoon [61]. Silk is mainly composed by the proteins mentioned above (fibroin and SS), presenting in its constitution natural impurities such as fats and inorganic salts [56].

SS is a highly hydrophilic protein that contains 18 amino acids. The presence of serine (≈32%), aspartic acid (≈18%) and glycine (≈16%) are the most significant, being glutamic acid, threonine and tyrosine also present [61],[62]. Its polar side chains have several functional groups (carboxyl, amine, hydroxyl) responsible for the moisturizing and oxidizing properties), allowing the interaction with other compounds through crosslinking, copolymerization or blending to form improved biomaterials [62],[63].

SS mainly adopts the form of an amorphous random spiral and may also present the form of a ß-sheet organized structure. The random spiral easily acquires ß-sheet conformation as a consequence of moisture absorption and mechanical elongation, forming a more dense, organized, crystalline and less soluble structure [60].

In addition to these characteristics, there are other important properties of SS (Table 4). If the protein is dissolved in hot water and subsequently undergoes a temperature decrease, its random coil structure becomes ß-sheet, acquiring a gelatinous form. That is, with the change in temperature the conformation of the protein changes. Upon heating the SS dissolves in solution, upon cooling the SS solution jellifies (Sol-Gel properties)[60],[61].

Table 4 - SS properties [55],[60],[64].

Properties	Characterization
Characteristics	White/yellow, odor free;
Solubility	Insoluble in cold water; Soluble in hot water;
Isoelectric point	Between 3,5-4;
Organic composition	Carbon (46,5%), oxygen (31%), nitrogen (16,5%), and hydrogen (6%);
Chemical formula	($C_{30}H_{40}N_{10}O_{16}$).

SS extraction

There are different methods to extract SS from silk filaments (different reaction types: acidic, alkaline, enzymes or even different conditions: time, temperature, pressure, pH) (Appendix C.1). The isolation method influences the solubility, molecular weight and gelling properties of the protein. According to the literature, the extraction of SS by boiling water is the simplest and cheapest method being, therefore the ideal for a simple approach [62].

Applications

The use of SS is increasing in a wide range of applications in food, cosmetic, biomedical and other industries (Appendix C.2) [65].

Recently, the association of bio organic compounds, such as biological macromolecules, with HAp has been a subject of great interest in the formation of biomaterials with improved properties. Many studies have shown that the presence of proteins in the system can greatly affect the crystallization of various CaPs [5]. In addition, these alterations may improve the biological response with respect to cell adhesion, cell proliferation and vascularization. Only a few studies addressed the use of HAp combined with SS (Appendix D). Nevertheless, the presence of this protein has shown to improve cell proliferation when used as an organic matrix or as a medium for cell growth [16],[66].

2.4.2 HAp/SS Nanocomposites

Nanoscale composites are known as nanocomposites. Nanocomposites present a high surface area, promoting better dispersion in the matrix and therefore an improvement of the physical properties of the composite that depend on the homogeneity of the material. Among these properties, there is greater mechanical resistance, lower permeability to liquids and gases, greater thermal stability and superior optical, magnetic and electrical properties [67],[12]. The components of a nanocomposite have an inorganic/inorganic, inorganic/organic or organic/organic nature. The HAp/SS nanocomposites are a new class of biomaterials, capable of offering microporous characteristics with high surface area which promotes the mechanisms of bone formation [17].

In the literature, the synthesis of HAp/SS products is not a very explored subject yet, but with a raising interest. The published works refer mainly to HAp/SS films and HAp/SS nanocomposites. The wet precipitation method for the synthesis of HAp/SS nanocomposites, using a ST is the most common. In addition to the required reagents, it is usual to use another reagent to adjust the solution pH. In the works published in the literature, SS is usually obtained by extraction in boiling water (Appendix C.1).

Chapter 3

Crystallization and Precipitation Processes

As for the Crystallization and Precipitation Processes chapter, the main theoretical principles of each process are described (namely supersaturation, nucleation, induction time, crystal growth and phase diagram). The differences between the two processes are also presented, being precipitation, the method used for the synthesis of the HAp/SS nanocomposites. The mechanisms, physical and chemical aspects of precipitation are also discussed.

3.1 Crystallization

Crystallization is the process by which crystals are formed from one or more substances in an amorphous, liquid or gaseous state. Precipitation of crystals from a solution is the most common form of crystallization. Although crystallization may occur during precipitation, the two terms are not identical. Precipitation simply refers to the formation of a solid substance (precipitate) from a chemical reaction. These processes are fundamentally characterized by three steps: supersaturation, nucleation and crystal growth [68].

3.1.1 Supersaturation

Most crystallization processes are aimed at creating a supersaturated solution. The supersaturation is the driving force of nucleation and crystal growth and determines the size distribution of the crystals. A solution is said to be saturated when in equilibrium with the solid phase at a given temperature. The term supersaturation refers to a solution which contains more solute than could be dissolved by the solvent, under normal circumstances [69], i.e., which contains a solute concentration higher than the saturation concentration (solubility limit) [36].

The fundamental driving force for crystallization can be defined by the difference between the chemical potentials of a given solute i in a supersaturated solution, μ_i, and in a saturated solution, μ_i^* , represented in equation (1.1):

$$\Delta\mu = \mu_i - \mu_i^* \quad , \tag{1.1}$$

being μ_i and μ_i^* defined in equation (1.2) and (1.3), respectively:

$$\mu_i = \mu_i^0 + RTlna_i = \mu_i^0 + RTln\gamma_i x_i \quad , \tag{1.2}$$

$$\mu_i^* = \mu_i^0 + RTlna^*{}_i = \mu_i^0 + RTln\gamma_i^* x_i^* \quad , \tag{1.3}$$

where μ_i^0 is the standard chemical potential of specie i, a_i is its activity in supersaturated solution, $a^*{}_i$ is its activity in saturated solution, γ_i is the activity coefficient, x_i its molar fraction in the solution, R is the gas constant and T is the absolute temperature.

The driving force for crystallization may therefore be expressed as descried in equation (1.4):

$$\frac{\Delta\mu}{RT} = ln\frac{a_i}{a_i^*} \tag{1.4}$$

However, since in most situations the solute activity coefficient is not known, supersaturation is usually expressed through the concentration driving force, ΔC (1.5), the supersaturation ratio, S (1.6), or relative supersaturation, σ (1.7) [70],[71]:

$$\Delta C = C - C^* \tag{1.5}$$

$$S = \frac{C}{C^*} \tag{1.6}$$

$$\sigma = S - 1 = \frac{C - C^*}{C^*} \, , \tag{1.7}$$

where C is the concentration of the solute in solution, and C^* is the equilibrium concentration (solubility).

3.1.2 Nucleation

The first formed solid embryos or nuclei that appear when the system is supersaturated mark the beginning of nucleation. This process defines the final size and the arrangement of the crystals. The condition of supersaturation alone is not sufficient to initiate crystallization, since this process requires the existence of a number of small solid bodies, embryos or nuclei, that act as centers of crystallization [37].

There are several mechanisms of nucleation. Primary nucleation refers to all cases of nucleation in systems that do not contain crystalline matter. This nucleation may be homogeneous (where the formation of the solid phase is spontaneous) or heterogeneous (where the formation of the solid phase is induced by the presence of other solid phases). Primary nucleation occurs essentially in precipitation systems or at the beginning of crystallization, while the number of crystals in the system is still low and supersaturation is very high [72]-[73]. On the other hand, nuclei can be generated nearby crystals present in the supersaturated system, this behavior characterizes secondary nucleation. All stirred crystallization systems promote secondary nucleation, as long as they contain crystals or other suspended solids (Figure 5) [37],[73].

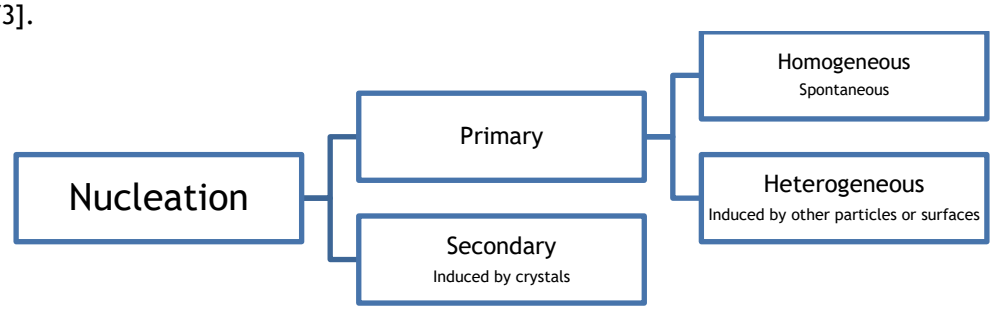

Figure 5 - Types of Nucleation [74].

Homogeneous nucleation

The process of forming a stable nucleus in a homogeneous fluid is still not fully understood. However, it is thought that it may result from a sequence of bimolecular additions, in which unstable molecules (clusters) of a given solute agglomerate (embryos) until reaching a critical size (1.8). Clusters smaller than the critical size are unstable and may disintegrate. If the addition mechanism extends beyond the critical cluster, crystal growth occurs, forming stable nuclei [37].

$$A+A=A_2;\ A_2+A=A_3\ \ldots\ldots\ A_n+A=_{An+1} \tag{1.8}$$

The formation of stable nuclei only happens if the activation energy or potential barrier, associated with the formation of an agglomerate of size r is exceeded, i.e., energy consumption is required to form a solid surface. At the same time, the loss of mobility within the solid leads to the release of energy [75]. Therefore, free energy variation for the formation of a new phase is represented by the free energy of Gibbs (ΔG) and results from the contribution of ΔG_s (free energy variation for the formation of the core surface) and ΔG_v (variation of free energy for phase transformation) (1.9) [74]:

$$\Delta G = \Delta G_s + \Delta G_V \tag{1.9}$$

For a spherical aggregate of radius r, surface tension γ and ΔG_v the free energy change of the transformation per unit volume has the following equation (1.10) [40]:

$$\Delta G = 4\pi r^2\gamma + \frac{4}{3}\pi r^3 \Delta G_v \quad (1.10)$$

Consequently, ΔG increases with r, until it reaches a maximum value known as activation energy (ΔG_{crit}). ΔG_{crit} corresponds to the critical size of the nucleus (r_c), which represents the minimal size of a nucleus which needs to be gained before the new phase is formed. After exceeding r_c the ΔG required will decrease to get a stable nucleus that can continuously grow into crystals (Figure 6) [6].

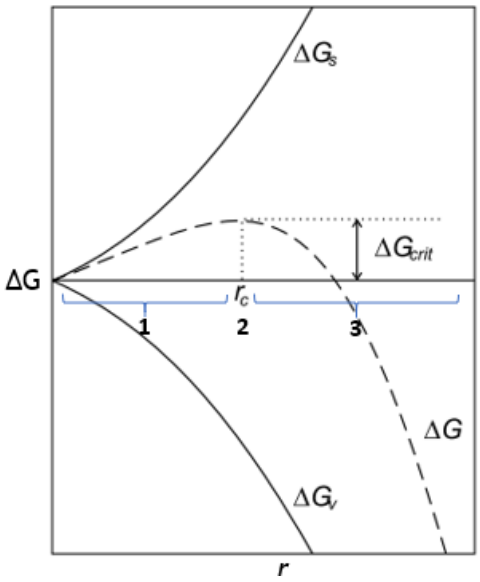

Condition	Effect
1 - r<rc	The embryo is unstable and dissolves.
2 - r=rc	The embryo remains in equilibrium with the solution.
3 - r>rc	The embryo is stable and grows.

Figure 6 - Variation of ΔG with r and behavior of an embryo according to its size [37],[31].

The r_c for a spherical nucleus can be obtained calculating the maximum of ΔG. This is achieved from equation 1.11 as follows:

$$\frac{d\Delta G}{dr_c} = 8\pi r_c\gamma + 4\pi r_c^2 \Delta G_v = 0 \therefore \quad r_c = \frac{-2\gamma}{\Delta G_v} \quad (1.11)$$

The speed at which nucleation occurs (J) corresponds to the number of nuclei formed per unit time and per unit volume, given by the equation 1.12 [31]:

$$J = A \exp\left(\frac{-16\pi\gamma^3 v^2}{3K^3T^3 ln S^2}\right) \quad (1.12)$$

This equation indicates the three main variables of nucleation rate: T, S and γ. K is the Boltzmann constant (1.3805 x 10-23 J.K^{-1}), and A is a pre-exponential factor [35].

In practical terms, homogeneous nucleation is an uncommon event, since it is virtually impossible to obtain a solution completely free of solid particles [37].

Heterogeneous nucleation

Heterogeneous nucleation systems are generally induced by the presence of impurities, ions or neighboring surfaces. This process occurs at lower supersaturations compared with homogeneous nucleation, therefore a correction factor is needed. The Gibbs energy of the critical nucleus that forms through heterogeneous nucleation, ($\Delta G_{c,het}$) is given by the following expression (1.13) [6]:

$$\Delta G_{c,het} = f_c G_{c,hom} \ , \quad (1.13)$$

where $G_{c,hom}$ is the Gibbs free energy of critical nuclei in the homogeneous process and f_c is the geometric correlation factor that depends on surface tension and is generally lower than unity (1.14) [6].

$$f_c = \frac{(2+cos\theta)(1-cos\theta)^2}{4} \quad (1.14)$$

The contact angle between the crystalline deposit and solid surface (θ) can be determined by Young's relation, that takes into consideration the surface tensions at the 3-phase boundaries (1.15):

$$\gamma_{sl} = \gamma_{cs} + \gamma_{cl} cos\theta \Leftrightarrow cos\theta = \frac{\gamma_{sl}-\gamma_{cs}}{\gamma_{cl}}, \quad (1.15)$$

where γ_{sl} the solid-liquid interfacial tension, γ_{cs} the crystal-solid interfacial tension and γ_{cl} the crystal-liquid interfacial tension (Figure 7) [37].

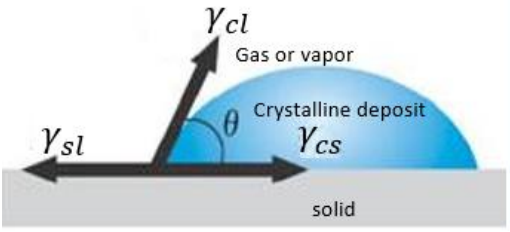

Condition	Interpretation
$\theta = 180°$	Complete non-affinity. Overall free energy of nucleation is the same required for homogeneous nucleation.
$0 < \theta < 180°$	Partial affinity. Nucleation is easier to achieve because the overall excess free energy required is less than for homogeneous nucleation.
$\theta = 0°$	Complete affinity. Supersaturated solution with crystals of the required crystalline product, i.e., no nuclei must be formed in the solution.

Figure 7 - Contact angle and interfacial tension [37].

Secondary nucleation

A supersaturated solution nucleates much more rapidly at lower supersaturation when solute crystals are already present in solution or are deliberately added (seeds). Secondary nucleation, besides being able to be originated by seeds can also be originated by intermediate layers (crystal-solution interface) and by contact (caused by friction). In the precipitation of poorly soluble substances, the contribution of secondary nucleation is overshadowed by primary mechanisms, only the latter being considered [6].

3.1.3 Induction time

The induction time (t_{ind}) represents the time that passes until the first nucleus is formed in the supersaturated solution. It can be decomposed into several parts: t_r (relaxation time), which is the time required for the system to achieve a quasi-steady-state distribution of molecular clusters, t_n which represents the formation of stable nucleus, and t_g that measures the time that elapses until the crystals become visible. The induction time decreases with the increase of the degree of relative supersaturation (1.16) [37].

$$t_{ind}=t_r+t_n+t_g \quad (1.16)$$

3.1.4 Crystal growth

Once the nucleus reaches the critical size, it begins to grow by adding and incorporating other molecules. There are several crystalline growth theories, being one of the most accepted provided by Kossel [37]. This model considers that the face of a seemingly smooth crystal is in fact composed of layers (steps) of monatomic height that may contain several kinks. On the

surface of the crystal there are adsorbed growth units (atoms, molecules or ions) and vacancies that can also be found in the steps between surfaces (Figure 8) [37].

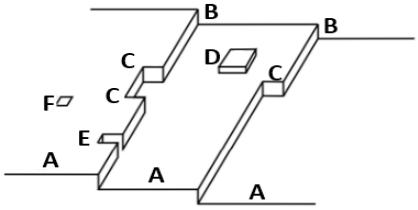

Figure 8 - A- Kossel's model of a growing crystal surface (A-flat surfaces; B-steps; C-Kinks; D- surface-adsorbed growth units; E-edge vacancies; F-surface vacancies) [37], [73].

According to Kossel model, growth units can attach to the surfaces, to steps or to kinks, forming one, two and three bonds, respectively. Hence, kink sites will offer the most stable configuration. The kink moves along the step and the face is eventually completed (Figure 9). A new step can be created by surface nucleation, this phenomenon is often started near the vertices of the crystal [37],[76].

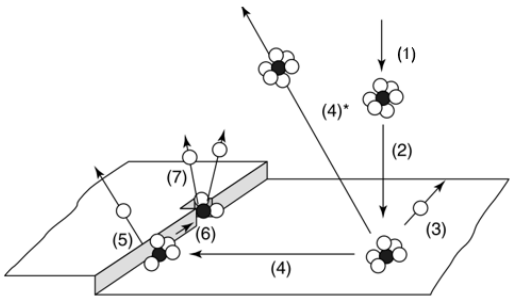

Figure 9 - Schematic representation of the processes involved in the crystal growth (1) Transport of solute to a position near the crystal surface; (2) diffusion through boundary layer; (3) adsorption onto crystal surface; (4) diffusion over the surface; (4*) desorption from the surface; (5) attachment to a step or edge; (6) diffusion along the step or edge; (7) Incorporation into kink site or step vacancy [76].

Crystalline growth process includes mass transport and integration and can be summarized through four stages: transport of atoms through solution, attachment of atoms to the surface, movement of atoms on the surface and attachment of atoms to edges and kinks [76].

To describe the effect of supersaturation on crystal growth rate, G, the following equation is used (1.16):

$$G = k_g \Delta C^g \ , \tag{1.16}$$

where k_g is the growth rate constant and g is the order of the overall growth process. k_g is temperature dependent and can be fitted to the Arrhenius equation, which can be rewritten, for growth rates, as a function of temperature as follows (1.17):

$$k_g = A \times \exp(\frac{-E_g}{RT}) \tag{1.17}$$

The activation energy can be used to obtain information of whether the rate controlling step is diffusion or surface integration (1.18):

$$G = A \times \exp\left(\frac{-E_g}{RT}\right) \Delta C^g \ , \tag{1.18}$$

where E_g is the activation energy of crystal growth [37].

3.1.5 Phase diagram

In a crystallization process it is important to know the solubility curve of the compound to be crystallized. The latter depends on several parameters, namely the solvent, pH, pressure and temperature. The solubility curve is generally plotted against two experimental parameters such as solute concentration and temperature (Figure 10). This type of diagram is called a phase diagram and allows defining the zones in which there may or may not be crystallization [36]:

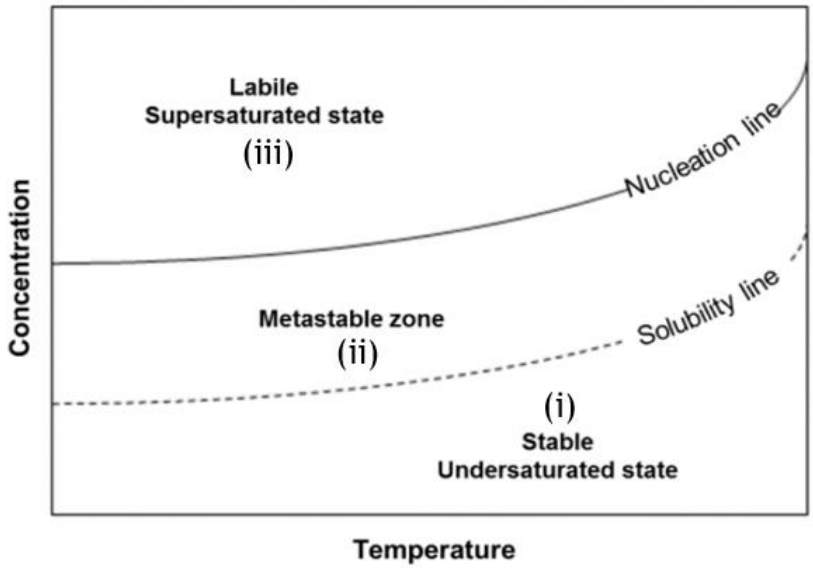

Figure 10 - Phase diagram [31].

As shown in Figure 10, the phase diagram is divided into three zones [36]:

i) The stable zone, where the solution is unsaturated, that is, the solute concentration in solution is less than its solubility, so that no crystals form;

ii) Above the stable zone and bounded by the solubility curve is the metastable zone, where the solution is supersaturated, but where the spontaneous formation of nuclei in the solution is impossible. In this region, it is only possible to form crystals by introducing a seed into the solution (crystal of the solute under study) or by mechanical disturbance of the solution;

iii) The labile or unstable zone corresponds to the zone where nucleation is spontaneous (nuclei are formed, and nuclei grow to form crystals).

3.2 Precipitation

3.2.1 Definition and stages

Precipitation can be seen in many cases as fast crystallization, although it may imply an irreversible process (when there is a chemical reaction). Precipitation is generally initiated at high supersaturations, which results in rapid nucleation and consequently the formation of many small crystals (Table 5) [37]. This process is widely used in industrial processes, laboratory techniques, analytical chemistry and in various fields such as metallurgy and geology [77].

Table 5 - Differences between crystallization and precipitation [5].

Process	Crystallization	Precipitation
Definition	Solid phase formation	Fast crystallization
Solubility	Large extension (medium to high)	Low
Achievement of supersaturation	Many forms	Dilution and reaction
Relative supersaturation	Low	High
Product Morphology	Well defined	Little defined (amorphous material)
Crystalline product size	Big	Little
Nucleation mechanism	Secondary	Primary
Nucleation rate	Low	High
Growth rate	Variable (0.005-0.5 μm. s^{-1})	Low (0,005-0,05 μm. s^{-1})
Control	Controllable	Difficult to control

Precipitation also consists of the three steps described above (supersaturation, nucleation and crystal growth). Usually these steps are followed by secondary steps, such as agglomeration or Ostwald maturation. These steps can cause major changes in the final product, namely in the crystal size distribution [37]. In fact, agglomeration consists of joining small particles to form larger particles to minimize their surface energy. Two types of agglomeration are generally distinguished: aggregation, i.e. the formation of a set of particles linked by physical forces (Van der Waals), and agglomeration, where the collision and aggregation of the particles are followed by formation of chemical bonds (Figure 11) [69].

Figure 11 - Schematic representation of the A-aggregation and B-agglomeration phenomena [74].

The key parameters in particle agglomeration include hydrodynamic conditions, particle size and the nature of the surrounding liquid. As for Ostwald ripening (Figure 12), it consists in the growth of larger crystals from those of smaller size, which have a higher solubility than the larger ones. Crystals formed initially slowly disappear, except for a few that grow larger, at the expense of the small crystals [69],[78].

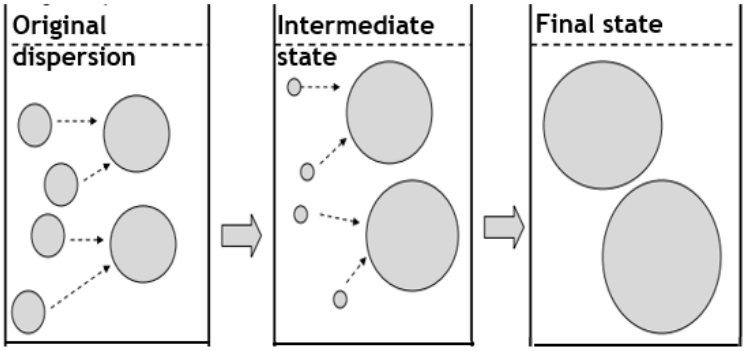

Figure 12 - Ostwald ripening effect [37].

3.2.2 Chemical aspects

In precipitation, the formation of the product may result from many consecutive reactions in solution, each with a different speed. According to the Ostwald Stage Law, the formation of a thermodynamically stable phase will be preceded by the formation of less stable (metastable) phases with higher energy than the stable phase, since that their formation occurs rapidly [79].

This phenomenon has already been verified during HAp precipitation, which is usually preceded by the formation of a metastable phase, such as amorphous calcium phosphate or octacalcium phosphate, depending on the operating conditions [4]. It is important to note the kinetics that occur during precipitation and to ensure that the kinetic equations refer to the reaction in question. In addition, the purity of a product applied as a bone substitute should also be controlled, since it is not intended to have side products (less stable, but more rapidly formed than HAp) that may be detrimental to cell growth [80].

3.2.3 Physical aspects

As already mentioned above, precipitation processes are characterized by the formation of many small particles, which generally have less than 1 μm in size. The behavior of such particles is governed by interfacial forces, which result from the balance between attractive van der Waals forces and repulsive electrostatic forces of the charged particles [78]. These forces can result in repulsion or attraction between particles. Thus, particles resulting from a precipitation process are usually secondary particles, i.e., particles resulting from the agglomeration of primary particles.

The mixing conditions also play a key role in the characteristics of the particles resulting from a precipitation process, since this type of process is characterized by high supersaturations and very fast chemical reactions and nucleation kinetics. For this reason, it is necessary to ensure an efficient mixing of the reaction system in order to provide a uniform distribution of supersaturation and thus a better control over the properties of the particles (such as their purity, phase, morphology and size distribution) [35].

Chapter 4

Reactors

This chapter summarizes the characteristics of the most commonly used reactors to produce HAp by precipitation, namely STs. Their characteristics and advantages are described, as well as their limitations. Finally, the meso-OFR is presented as an alternative to the conventional reactors to produce HAp nanocomposites. This reactor has shown significant increase in the intensification of mixing. Moreover, meso-OFR reduces reagent requirements and waste when used for research purposes and its scale can also be easily extended.

There are different ways of achieving supersaturation, such as cooling the saturated solution, evaporating the solvent, adding an antisolvent that reduces solute solubility (Drowning-Out) or promoting a chemical reaction leading to solute precipitation [69]. The chemical reaction is widely used to obtain HAp particles [81]. For this reason, in this chapter the reactors used to precipitate HAp will be discussed. Most industrial and laboratory precipitation units are simple to construct. The main purpose is to mix the reactants rapidly to allow the formation of a precipitate with the desired physical and chemical characteristics [37].

4.1 Stirred tank reactor

4.1.1 Stirred tank batch reactor (ST)

The most common operations are those that use a ST, where the reactants are introduced into the reactor, and after the reaction, the products are collected. A typical batch reactor consists of an agitator and an integrated temperature control system (Figure 13 A). The main advantage of this system is its versatility, which can be used in solids dissolution, product mixing, chemical reactions, crystallization, among others. Furthermore, the stirred tank reactor is easy to implement and has acceptable production costs [82]. However, the use of this type of system has disadvantages, being characterized by heterogeneous distributions of parameters such as temperature and concentration, leading to heterogeneous distribution of supersaturation in the reaction medium. This affects the reproducibility and the quality of the product formed. Although macromixing is achieved by stirring, micromixing, which refers to stirring at the molecular level, is not controlled [31]. ST can also be operated in semi-batch or continuous mode [83].

4.1.2 Stirred tank semi batch reactor (STS)

An example of another type of reactor is the STS. This works in a similar way to the batch reactor, because the reaction occurs in a single stirred tank. However it is modified to allow the addition of reagents and/or the removal of the product in a certain time, that is, allows the partial addition of reagents with the flexibility to add more as time progresses (Figure 13 B) [84].

4.1.3 Continuous stirred tank reactor (CSTR)

CSTRs are also utilized because they allow a more efficient use of the reagents and a greater control over the operative parameters such as the temperature and the concentration of the reagents, thus allowing to obtain a more uniform product. One of the disadvantages of this type of reactor is the deposition of reaction products, which occurs after some time of operation, leading to the frequent need to stop the process and wash the reactor. In addition, this type of reactor does not guarantee homogenization and adequate mixing of the reactants, which generally results in the formation of particles with a large size distribution (Figure 13 C) [85].

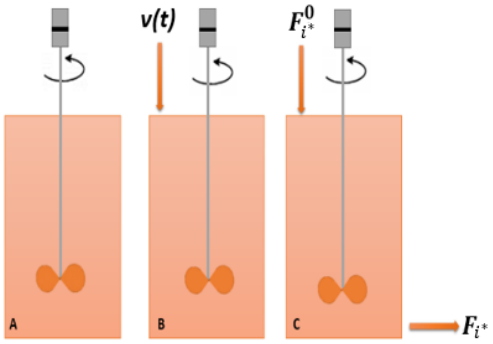

Figure 13 - A) ST; B) STS, where v(t) is the flow rate that can vary over time; C) CSTR (Volume V, at temperature T, is the same throughout the reactor and at any time. F_{i*}^0 is the molar flow rate of species i^* in the reactor, while F_{i*} is the molar flow rate of species i^* outside the reactor [84].

Due to the limitations of the systems described above, several reactors have been developed in order to better control the reaction conditions, and thereby optimize the characteristics of the final product [84].

4.2 Microreactors

Recently, microreactors were applied to precipitate HAp in order to overcome the problems associated with STs solution mixture. Transfer processes, mixing of reactants as well as residence time occur faster in these devices. This is due to the scale reduction of the reactors, which allows a better control over the reaction medium [86]. Several configurations have been applied (Table 6).

Table 6 - Different types of reactors used to obtain HAp.

Microreactor			Ref.
Name	**Description**	**Scheme**	
T-junction microchannel reactor	Two feed channels and one reaction channel converge at the T-junction, where the reactants impinge and then flow through the reaction channel as the reaction proceeds.	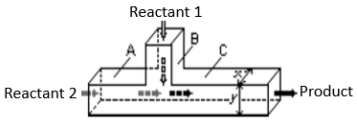	[87], [88], [89]
NETmix (Network mixing) reactor	Network of several mixing chambers interconnected by channels. Reactants are injected at the inlet channels. Mixing occurs in these chambers when the two streams coming from each channel meet.	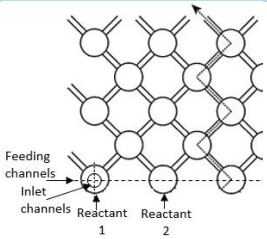	[83], [90], [91]

Microreactors are usually characterized by geometries with a low Reynolds number (Re). Reynolds number is the ratio of inertial forces to viscous forces and is a convenient parameter for predicting the physical characteristics of the flow (2.1) [92].

$$\mathrm{Re} = \frac{inertial\ forces}{viscous\ forces} = \frac{\rho.V.D}{\mu}\ , \qquad (2.1)$$

where ρ is the fluid density (kg/m^3), V is the flow velocity (m/s), D is the diameter (m) and μ the dynamic viscosity (Pa.s = kg/(m.s)).

When Re is large, inertial forces dominate over the viscous forces, the fluid is flowing faster and the flow is turbulent (Figure 14 A). On the other hand, when Re is low, the viscous forces are dominant, and disturbances in the flow are damped out by viscosity. In this case, fluid particles are kept in line generating a laminar flow (Figure 14 B) [92].

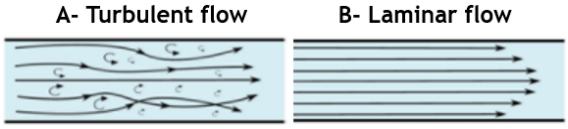

Figure 14 - Flow regimes (A) turbulent flow; (B) laminar flow [93].

In microreactors channels, laminar flow is dominant and is characterized by a parabolic velocity profile, leading to residence time distributions. The parabolic velocity profile or obstruction limit the use of these reactors [31]. Furthermore, it is difficult to find practical industrial applications for these reactors as the product quantity is very small [94].

4.3 Meso oscillatory flow reactor (meso-OFR)

In an oscillatory flow reactor (OFR) the fluid is typically oscillated in the axial direction by means of diaphragms, bellows or pistons. The reactor column contains uniformly spaced orifice deflectors (Figure 15). The intensity of the mixture is controlled by the frequency and amplitude of the fluid oscillation. This reactor has been studied in chemical engineering processes such as crystallization, and has been shown to provide effective and uniform mixing [95].

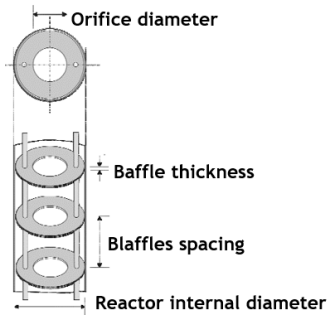

Figure 15 - Schematic representation of cross section in an OFR [95].

The OFR has perpendicular sharp edges to a periodic and fully reversing flow that accelerates and decelerates according to a sinusoidal velocity–time function. The oscillatory flow mixing acceleration is characterized by the formation of vortices, which are generated by the interaction of the flow with the baffles. Vortex rings are formed downstream of the baffles. When the flow decelerates these vortices move into the center of the reactor, where a well-mixed and uniform region is generated (Figure 16). Mixing control can be achieved by a combination of different geometric parameters and operational parameters (baffle area, baffles spacing, baffle thickness, frequency and amplitude in the flow patterns and power input) [95]. Comparing a conventional tubular reactor and an OFR, the main difference is that in the OFR mixing intensity can be controlled through oscillating conditions, influencing the size and frequency of vortex formation, not by altering the flow rate [96].

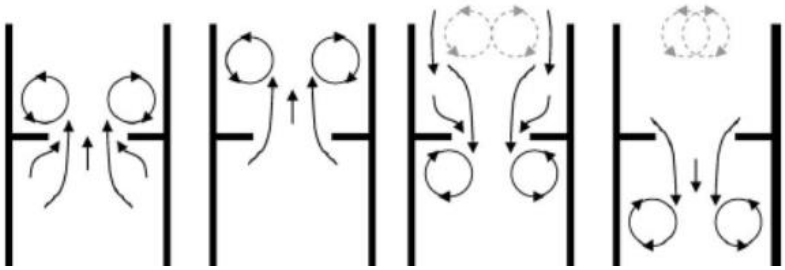

Figure 16 - Mechanism of oscillatory flow mixing (OFM) in an OFR [97].

The mechanical conditions of a fluid in an OFR are represented by the oscillatory Reynolds number (Re_0), that describes the intensity of mixing applied to the tube (2.2), and the Strouhal number (St), represents the ratio of tube diameter to stroke length, measuring the eddies propagation (2.3).

$$\mathrm{Re}_0 = \frac{w\rho x_0 D}{\mu} = \frac{2\pi f x_0 \rho D}{\mu} \ , \tag{2.2}$$

$$\mathrm{St} = \frac{D}{4\pi x_0} \ , \tag{2.3}$$

where w is the angular frequency of oscillation (rad/s) (=$2\pi f$), f is the oscillation frequency (Hz) and x_0 the oscillation amplitude center-to-peak (m).

Despite its advantages, conventional OFR presents limitations associated with the existence of dead zones or stagnate regions near the angle between the baffles and the reactor [71]. There are several types of baffles geometry that have been studied in alternative to the sharp edges design [98]. Due to the problems associated to conventional OFR, a new meso-OFR was developed by the Laboratory of Process Engineering, Environment, Biotechnology and Energy (LEPABE) from Faculty of Engineering of Porto (FEUP) and the Centre of Biological Engineering (CEB) from University of Minho [20]. The changes made aimed at reducing the problems associated to conventional OFRs. The meso-OFR consists in a glass tube provided with smooth periodic constrictions, operating under OFM, where mixing intensity is controlled by f and x_0. The meso-OFR was also scaled-down from the typical 1-15 cm of inner diameter to 3 mm. It is a reactor with about 4 mL of volume and 35 cm of length (Figure 17). The new meso-OFR has shown a significant increase in the intensification of mixing in multiphase systems, and its scale can also be easily extended [19].

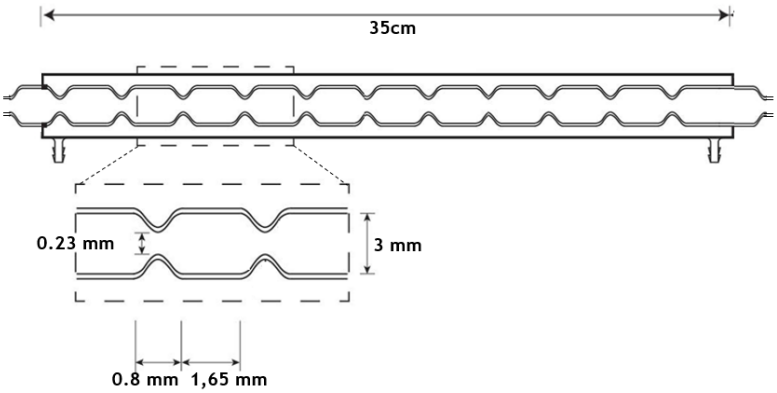

Figure 17 - Geometry of the meso-OFR [20].

Chapter 5

Materials and Methods

The experimental activities took place in LEPABE, except for SS extraction, which was carried out in the Centre for Biotechnology and Fine Chemistry (CBQF) at the Faculty of Biotechnology of the Catholic University of Portugal (ESB).

5.1 Materials and Reagents

The synthesis of HAp/SS nanocomposites was carried out in batch in two different reactors, a stirred tank reactor (ST) and in the meso-oscillatory flow reactor (meso-OFR), developed in LEPABE [20]. The nanocomposites were synthesized by mixing equal volumes of a solution of calcium chloride dihydrate ($CaCl_2.2H_2O$) (Merck, 99.5%), in which a certain volume of SS solution was dissolved, with a solution of disodium hydrogen phosphate (Na_2HPO_4)(Sigma-Aldrich, 99.0%). Both solutions were prepared with ultrapure water (18.2 $M\Omega.cm^{-1}$ at 25 ºC) and heated to 37 ºC. pH calibration was made with two buffer solutions (Hanna Instruments) with pH 7and 4 at 20 ºC.

Commercial HAp (Spectrum, Calcium Hydroxyapatite, Powder, Minimum 40 Mesh) and lyophilized SS (APPACDM, Castelo Branco, Portugal) were analyzed in some characterization techniques to allow comparison with the obtained particles.

5.2 Description of the experimental set-ups

5.2.1 ST

The ST reactor consists of a jacketed cylindrical vessel made of glass, with 19 cm in height and 8,7 cm in diameter. The reactor has an approximate volume of 200 mL. Stirring is ensured by a metal stirrer driven by a motor (R50C, CAT) kept at 300 rpm (Figure 18 A).

5.2.2 Meso-OFR

The meso-OFR consists of a 35 cm long and 3 mm internal diameter glass jacketed tube provided with smooth periodic cavities (SPC), with an approximate volume of 4 mL. The

agitation was ensured by the oscillations of the fluid inside the reactor, being x_0 and f fixed at 4,5 mm and 110 rpm, respectively (Figure 18 B). The crystallization solution was oscillated using a piston moved by a stirring motor (CATR100C, United States of America). The oscillating device was custom-built.

Both reactors are jacketed and were connected to a thermostatic bath (37 °C) (Tectron-Bio, JPSELECTA) for temperature control. The experimental set-ups were also equipped with a pH electrode (Sentek, P11 / HA for the ST and SenTix Mic-D, WTW for the meso-OFR) and a temperature sensor (TFK 325, WTW) for the monitoring of the precipitation experiments.

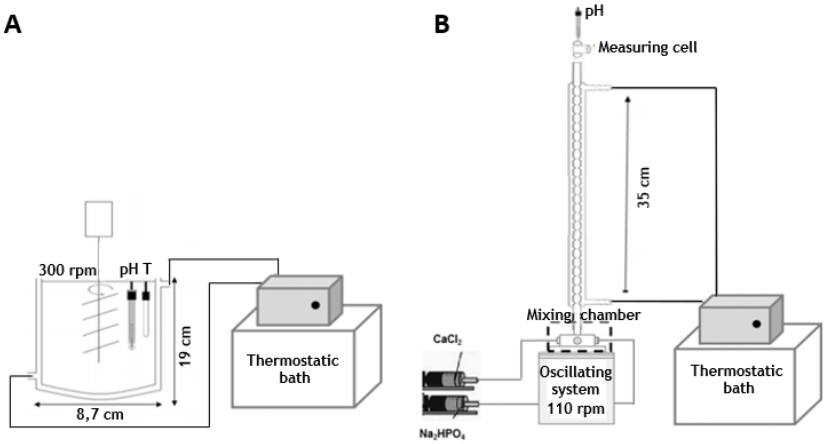

Figure 18 - Experimental set-ups for the precipitation of HAp/SS nanocomposites (A) ST (B) meso-OFR.

5.3 SS extraction

There are different methods to extract SS from silk filaments, being the degumming process by boiling in water the simplest procedure, as described in chapter 2. SS was extracted from cocoons of the *Bombyx mori* silkworm acquired from APPACDM. Then the cocoons were cleaned, cut into small pieces of approximately 1 cm and weighed to reach 5 g. 500 mL of ultrapure water (18,2 MΩ.cm^{-1} at 25 ºC) were boiled and the pre-prepared cocoons were added. The solution remained boiling for 1 hour with constant magnetic stirring (150 rpm). After the extraction time elapsed the solution was filtered (Coffee filter SELEX nº4), being obtained approximately 100 mL of SS solution with a concentration of 3 g.L^{-1} (Figure 19).

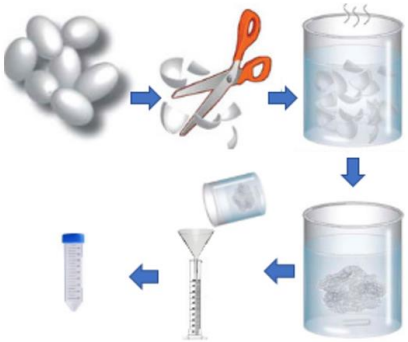

Figure 19 - Representative scheme of the SS extraction process in boiling water.

5.4 Synthesis of HAp/SS nanocomposites

The initial Ca/P of the reactants used was 1,67. According to the reactants and Ca/P used it is expected that the CaP phase formed is HAp (5.1):

$$10CaCl_2 + 6Na_2HPO_4 + 2H_2O \rightarrow Ca_{10}(PO_4)_6(OH)_2 + 12NaCl + 8HCl \qquad (5.1)$$

Different concentrations of SS were tested (0,1 g/L and 1 g/L) (Table 7). For each experimental condition, three replicates were performed.

Table 7 - Operating Conditions studied.

Sample	[$CaCl_2.2H_20$] (M)	[Na_2HPO_4] (M)	Sericin (SS) (g/L)	Temperature (°C)
HAp	0,02	0,012	-	37
HAp/SS1			0,1	
HAp/SS2			1	

In the ST, precipitation was started by the quick addition of the solution of $CaCl_2.2H_2O$ and SS to the solution of Na_2HPO_4, for about 10 s. Regarding the meso-OFR, the reactants were fed into the set-up one at a time by means of a syringe pump (NE-4000, New Era, EUA) using syringes of 5 mL (BD Plastipak). The solution of Na_2HPO_4 was slowly injected to prevent the formation of bubbles (Q = 2 mL/min). Afterwards, the solution of $CaCl_2.2H_2O$ and SS was injected (Q = 9 mL/min).

5.5 Sample Characterization

Precipitation processes of HAp/SS nanocomposites in both reactors were assessed through the comparison of pH profiles and particles characteristics (Figure 20).

In the ST the suspensions were collected and filtered (0,2 µm pore size membrane, Gelman Sciences, USA), while in the meso-OFR the suspensions were centrifuged (20 min, 70 x 100 rpm) due to the limited quantity of sample available. In both cases the samples were washed with ultrapure water and ethanol (to stop the solid-liquid reaction) and dried in the oven for 24 hours at 70°C.

For the Laser granulometry, the suspensions were directly collected from the reactor for the analysis, whereas for the other characterization techniques (FTIR, XRD, SEM, TEM and STEM) powder samples were used.

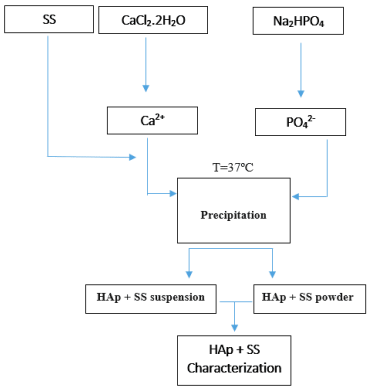

Figure 20 - Flowchart of the method for the preparation of HAp/SS nanocomposites.

pH profile

For each experimental condition, the pH of the reaction medium was measured over time. The acquisition of data was made through LabVIEW. Three trials were performed for each experimental condition with the duration of approximately 4h in the ST and 2h 30 min in the meso-OFR. The variation of pH over time allows the monitorization of the precipitation reaction, being the stabilization of the pH an indication of the end of the reaction and of the

formation of stable nanocomposites [21]. Furthermore, pH is an important parameter for determining the probability of formation of intermediate phases of CaPs [31].

FTIR (Fourier-transform infrared spectroscopy)

FTIR allows the identification of functional groups, producing a profile which can be seen as the fingerprint of the sample analyzed [99]. For the identification and comparison of the samples, the FTIR (Fourier-transform infrared spectroscopy) (ALPHA II FTIR, Bruker) spectra of a commercial HAp and lyophilized SS were analyzed, performing 12 scans in absorbance mode. In addition, the reference spectra presented in the literature [100],[66] were consulted. The comparison of the FTIR spectra and the identification of the functional groups were done using Essential FTIR.

XRD (X-Ray Diffraction)

XRD is performed for phase identification and crystallinity of the sample [101]. The XRD (X-Ray Diffraction)(PanAlytical X'Pert PRO Alfa-1 diffractometer with λlCuKa=1.54056 ˚A) patterns of the different experimental conditions studied in the ST were compared with the commercial HAp and with the standard XRD reference of the HAp (JCPDS 00-009-0432) [31].

Laser granulometry

Laser granulometry provides the particle size distribution. Laser diffraction particle size analyzers provide indirect size measurements of spherically equivalent particles [102]. For particle size distribution (LS 230, Beckman Coulter), the suspensions produced were directly analyzed from the system without thermal treatment and without granulometric separation. The analyses were made using ethanol as solvent. The particle size distributions in volume and number were used for the studied particles, to detect the presence of aggregates and to study the size of most particles, respectively [31]. The distributions obtained were compared with the distributions obtained for the commercial HAp.

SEM, TEM and STEM (Scanning electron, Transmission electron and Scanning Transmission microscopy)

The size and morphology of the obtained particles was assessed by different electron microscopy techniques. SEM (Scanning electron microscopy) (FEI Quanta 400FEG ESEM/EDAX Genesis X4M with an accelerating voltage of 15 kV and 20 kV) allowed the visualization of the 3D structure of the sample [1]. EDS (Energy Dispersive X-ray Spectrometry) was used to obtain the elemental composition of the analyzed particles[103]. The samples were mounted on a stub of metal with carbon tape and covered by a 10 nm layer of gold. While from the obtained TEM (Transmission electron microscopy) (TEM JEOL, 2200 FS / EDS Oxford, INCA Energy TEM 250) images it was possible to visualize the size and morphology of smaller particles, in particle nanosized particles. The images obtained are 2D but compared to SEM, the resolution is higher.TEM also allows to analyze the crystallinity of the sample [1], through SAED (selected area electron diffraction). SAED, is an electron diffraction technique which provides crystallographic information through ring patterns [104]. STEM (Scanning transmission electron microscopy) (Hitachi HD-2700) combines concepts from SEM and TEM. In addition to the increase in spatial resolution, it also provides an increase in contrast in the acquired images. This technique is suitable for the detection of small differences in structure and composition

of a sample. EDS can also be obtained in STEM [105]. For TEM and STEM analysis, a low concentrated suspension of the powders was prepared in ethanol and placed on a copper grid (StrataTek, Square Mesh Grids, 400 mesh, Copper).

5.6 - Comparison of the HAp particles obtained with those of the NETMIX reactor

Comparison of the particles obtained with commercially available HAp particles is important to evaluate the viability and advantages of the suggested methodology for the synthesis of HAp/SS nanocomposites. For this, the characteristics of the particles obtained were compared with those of the particles obtained in the NETmix reactor, in terms of morphology, size, crystallinity, purity and stoichiometry. The Netmix reactor is used in Fluidinova.S.A, which is the only company in Portugal responsible for the manufacture and supply of synthetic nano-HAp [106].

Chapter 6

Results and Discussion

6.1 pH profile

From a thermodynamic point of view, the experimental conditions chosen favor the precipitation of HAp, since for pH between 4 and 12 and at 37 ºC, this is the less soluble CaP. However, considering the kinetic factors, HAp is not the only CaP that can be formed [86]. Considering this, the precipitation of CaPs from supersaturated solutions is a complex phenomenon, since several intermediate phases can precede the formation of the most thermodynamically stable phase [39],[107]. Several reports refer to the formation of intermediate precursors in HAp precipitation systems [108]. ACP is predominantly formed at pH>7, followed by subsequent nucleation of OCP which serves as a template for HAp formation. At lower pH the formation of HAp is observed to be preceded by OCP or DCPD [109],[80].

According to the results, the pH profiles of the different experimental conditions studied for the ST are quite similar (Figure 21 A), differing only in the first instances (Figure 21 B).

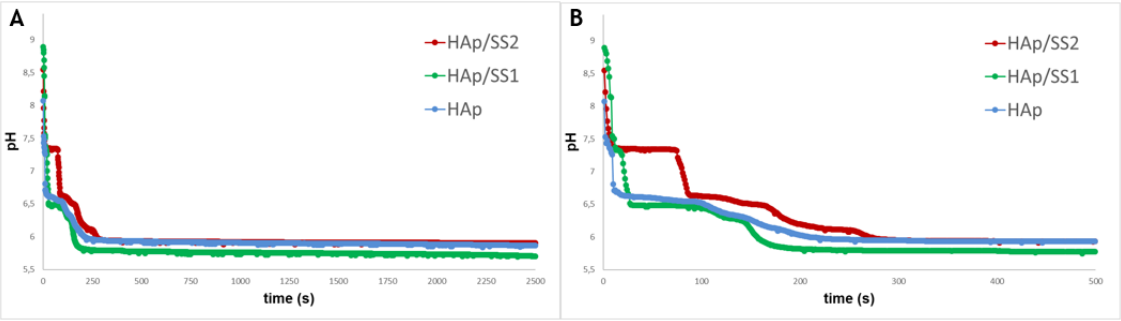

Figure 21 - Variation of pH over time for the experimental conditions studied in the ST for the entire experimental time (A) and for the first 500 s (B).

For all the experimental conditions, six stages were identified (Figure 22). In the first stage the pH decreases abruptly when $CaCl_2.2H_2O$ is added. In the second stage the pH is approximately constant, which may indicate the formation of an intermediate CaP phase. In

the third stage a decrease in pH is observed, which may correspond to a phase transformation, i.e. the passage of the CaP formed in stage two to another CaP. The fourth stage is approximately constant, while the fifth stage is marked by a slow decrease in pH. Finally, the sixth stage corresponds to pH stabilization, which means that the CaP formed is stable (Figure 21 and Figure 22). The following equations represent the steps that may have occurred during the experimental activity, namely the formation of ACP in the second stage (5.2), OCP in fourth stage (5.3) and HAp in the sixth stage (5.4).

$$3CaCl_2 + 2Na_2HPO_4 + 2H_2O \rightarrow Ca_3(PO_4)_2.2H_2O + 4NaCl + 2HCl \quad (5.2)$$

$$3Ca_3(PO_4)_2.2H_2O + 2H_2O \rightarrow Ca_8H_2(PO_4)_6.5H_2O + Ca^{2+} + H_2O \quad (5.3)$$

$$5Ca_8H_2(PO_4)_6.5H_2O \rightarrow 4Ca_{10}(PO_4)_6(OH_2) + 6H_3PO_4 + 17H_2O \quad (5.4)$$

It is also possible to verify that the first three stages are shorter in the absence of SS. The HAp/SS2 experiment has longer initial stages. The remaining stages are identical for all conditions. The pH variations in the different stages are similar for all experimental conditions (Appendix E).

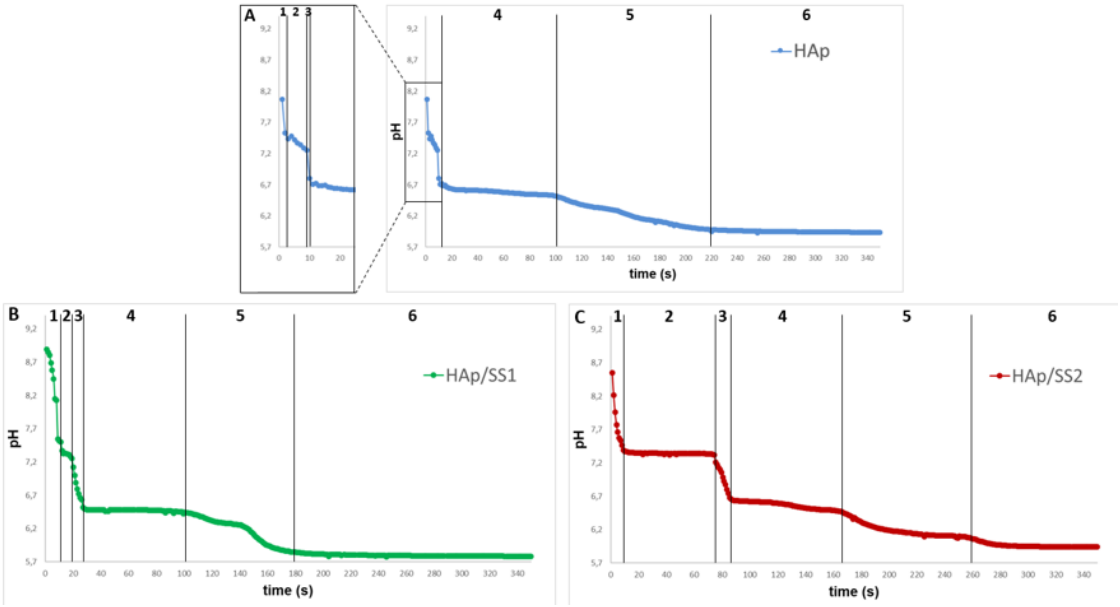

Figure 22 - Stages identified in the ST pH profiles for (A) HAp (B) HAp/SS1 and (C) HAp/SS2.

Regarding the meso-OFR, the results show that the pH profiles are also similar for all the experimental conditions (Figure 23 A). Unlike the ST, it is not possible to distinguish different stages in the pH profiles obtained (Figure 23 B). The pH profiles are characterized by a gradual decrease of pH until its stabilization.

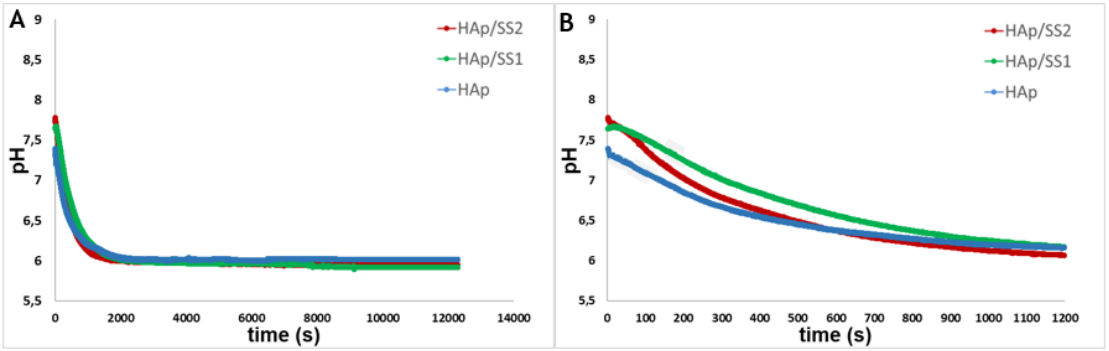

Figure 23 - Variation of pH over time for the experimental conditions studied in the meso-OFR for the entire experimental time (A) and for the first 2500 s (B).

In the ST, the pH stabilizes around 5.6 after approximately 2 h for the three conditions tested (Figure 21 A), while in the meso-OFR the pH stabilizes around 6 after approximately 2000 s (≈ 33 min) ((Figure 23 A), meaning that HAp precipitation process is about four times faster in the meso-OFR. Furthermore, in the meso-OFR, as the formation of different stages did not occur, this can mean that no intermediate CaP is formed.

6.2 FTIR

FTIR was performed for all the samples obtained, as well as for a commercial HAp and SS. According to the bands identified in the spectra of the particles formed in the ST and in the meso-OFR, all the samples show the typical structure of HAp [100]. In addition, FTIR spectra of the samples containing SS evidence bands assigned to amides, confirming thus its presence in the samples (Figure 24 and Figure 25). The identified bands were compared to data presented in the literature regarding HAp [100] and SS [66] (Table 8).

Concerning the ST, most of the bands attributed to phosphate groups (PO_4^{3-}) were identified in all the samples. In the spectra of the HAp/SS1 and HAp/SS2 samples it is possible to identify a peak at 1639 cm^{-1} and 1633 cm^{-1}, respectively. This peak can be attributed to amide I and as expected its intensity increases with the SS concentration. In addition, the presence of amide II is visible in the spectra of both samples (HAp/SS1: 1517 cm^{-1} and HAp/SS2: 1519 cm^{-1}), while the presence of amide III is only visible in the HAp/SS2 spectrum (1407 cm^{-1}) (Figure 24 and Table 8). In the literature, a higher concentration of sericin in HAp/SS nanocomposites synthesized in a ST, was also associated with a higher intensity of SS characteristic peaks [66].

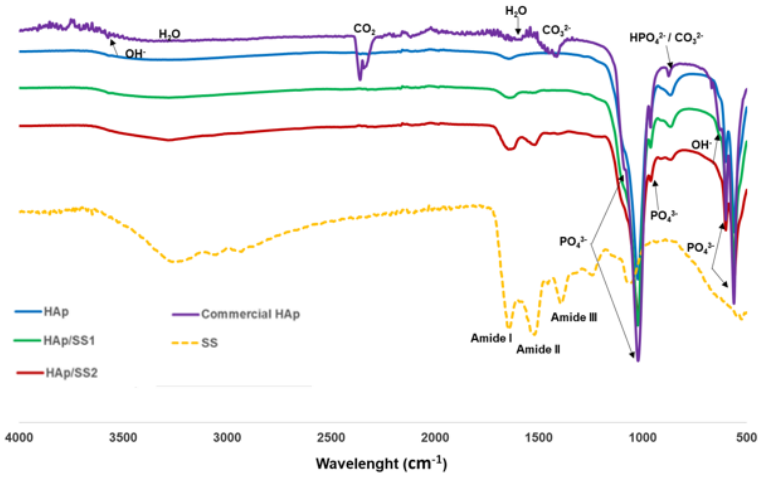

Figure 24 - FTIR spectra of the particles produced in the ST.

In the spectra of the samples formed in the meso-OFR, although the characteristic bands of HAp are identified, it is possible to verify that their intensity is lower when compared to commercial HAp and to the particles obtained in the ST (Figure 25). This may indicate that the particles synthetized in the meso-OFR are less crystalline.

The pH changes during the precipitation process alter the relative concentrations of the several ionic forms of phosphoric acid ($H_2PO_4 \rightleftharpoons H_2PO_4^- \rightleftharpoons HPO_4^{2-} \rightleftharpoons PO_4^{3-}$), thus changing the chemical composition of the CaP formed [110]. HAp and HAp/SS1 particles obtained in the meso-OFR have a peak at 1215 cm^{-1} assigned to hydrogen phosphate (HPO_4^{2-}) ions. In addition, most of the samples obtained in both reactors show a peak around 875 cm^{-1}, which can be attributed to HPO_4^{2-}. HPO_4^{2-} may have replaced the PO_4^{3-} ions [111], suggesting thus that the formed CaP are calcium deficient HAp (OHAp). OHAp is susceptible of surface adsorption and

lattice substitutions [39]. Also, this may explain why it was not possible to identify the OH^- peak (632 cm^{-1}), since the presence of HPO_4^{2-} ions can be related to Ca^{2+} and OH^- ion vacancies ($Ca_{10-x-y}(HPO_4)_x(PO_4)_{6-x}(OH)_{2-x-2y}$, where x can decrease from 1,1 to 0,03 and y is relatively constant at approximately 0,5) [39].

The samples HAp and HAp/SS1 present a large amount of water. For this reason, it is difficult to identify the peak assigned to amide I in the HAp/SS1 spectrum. Regarding HAp/SS2, less adsorbed water is present in the spectrum, therefore it is easier to identify the peak assigned to amide I (1638 cm^{-1}). The peak related to amide II can be identified in both HAp/SS1 (1410 cm^{-1}) and HAp/SS2 (1542 cm^{-1}) spectra (Figure 25 and Table 8). Considering its properties, SS should be associated with the adsorption of a greater amount of water, i.e., an increase of the hydrophilicity of the particles. This is not verified for the HAp/SS2 condition in the meso-OFR, probably due to some change in the collecting method of an experimental activity.

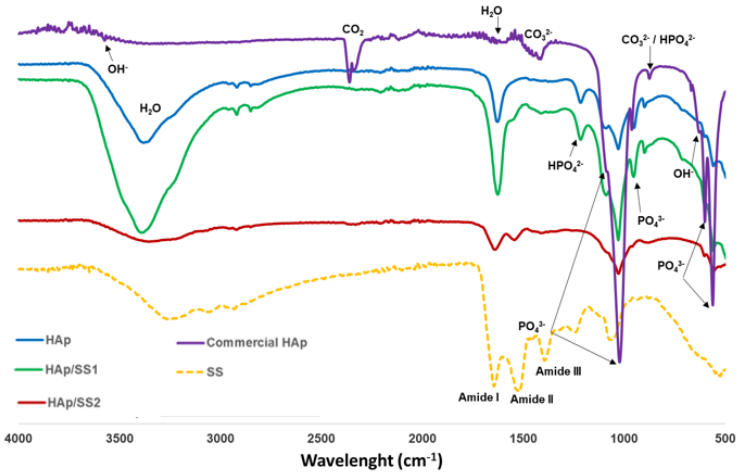

Figure 25 - FTIR spectra of the particles produced in the meso-OFR.

For all the samples, the hydroxyl group (OH^-) at approximately 3573 cm^{-1} is not evident since there may be an overlap with the band corresponding to adsorbed water (3000-3700 cm^{-1}) [100]. As for the vibrational mode at 632 cm^{-1} [100], it is not visible in all the FTIR spectra.

The presence of adsorbed water can be associated with the low drying temperatures (70°C) and the absence of thermal treatments of the samples. One can also observe that the presence of adsorbed water in the particles formed in the meso-OFR is higher when compared to the particles formed in the ST. This can be justified by the fact that the particles obtained in the meso-OFR were collected by centrifugation and not by filtration as in the ST, and thus the quantity of mother liquor that remains is higher.

The presence of the carbonate group (CO_3^{2-}) can be justified by the dissolution of atmospheric CO_2 in the reaction medium [100]. As a consequence, the partial replacement of the PO_4^{3-} ions by the CO_3^{2-} ions in the structure of HAp may occur [112]. In this way, the reactors were partially capped during the experimental activities to minimize the presence of carbonate ion.

Table 8 - Identification of the functional groups present in the FTIR spectra of the samples obtained in the ST and the meso-OFR [100],[66].

		Wavelength (cm^{-1})								
Reactor	Sample	PO_4^{3-}	HPO_4^{2-}	CO_3^{2-}	H_2O	CO_2	OH^-	Amide I	Amide II	Amide III
	HAp and SS reference [100], [66]	1087, v_3 1032, v_3 962, v_1 602, v_4 561, v_4 472, v_2	1215	875 1410	3800-3000 1630	2300	631 3572	1657	1551	1251
	Commercial HAp	1089 1022 962 600 561 472	--	875 1413	≈3700-3000 1631	2359	632 3573	--	--	--
	SS	--	--	--	≈3700-3000 1631	--	--	1645	1520	1242
ST	HAp	- 1022 962 601 559 --	865 --	--	≈3700-3000 1643	--	--	--	--	--
	HAp/SS1	-- 1026 962 601 561 --	865 --	--	≈3700-3000 1639	--	--	1639*	1517	--
	HAp/SS2	-- 1022 962 590 559 --	864 --	--	≈3700-3000 1633	--	--	1633*	1519	1407

Meso-OFR	HAp	1089 1029 950 600 557 --	899 1215	--	≈3700-3000 1627	--	--	--	--	--
	HAp/SS1	1089 1029 950 600 557	899 1215	--	≈3700-3000 1625	--	--	--	1410	--
	HAp/SS2	-- 1028 961 601 557	--	--	≈3700-3000 1638	--	--	1638*	1542	--

6.3 XRD

Through XRD analysis it was possible to verify that the peaks observed in the XRD patterns of the samples formed in the ST are in agreement with the XRD pattern of HAp (Figure 26 and Table 9). The crystallinity of all the samples obtained is low, in comparison to the commercial HAp, once all the XRD patterns present broad peaks with low intensity. These characteristics are found in poor crystalline and small size particles (nano particles), being similar to biological HAp [42],[113]. There was no perceptible change in the crystallinity of the samples with the increase of SS concentration. In the literature, SS incorporation gave rise to lower crystallinity in HAp/SS nanocomposites, when compared to HAp [66]. The XRD patterns obtained are noisy which may have prevented the distinction of phase distortions.

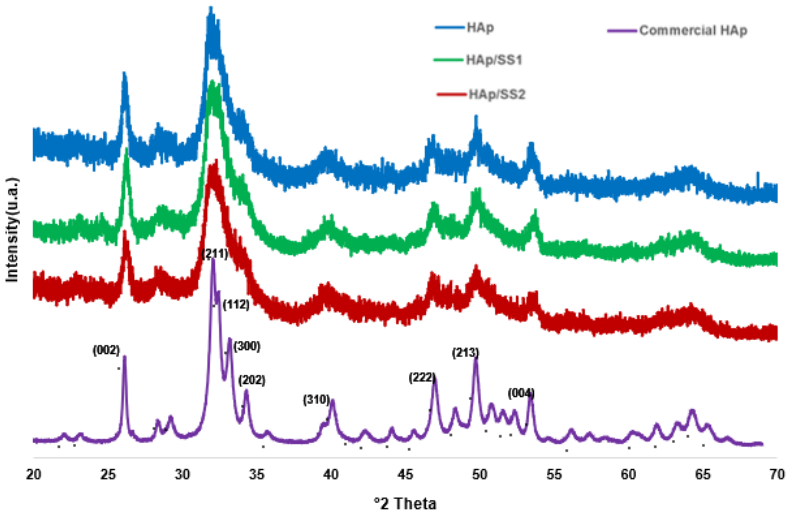

Figure 26 - XRD patterns of the particles produced in the ST.

Table 9 - Identification of the peaks present in the XRD patterns of the samples obtained in the ST.

Sample	**°2 Theta**					
Miller Index	HAp reference (JCPDS 00-009-0432)	Commercial HAp	[100]	HAp	HAp/SS1	HAp/SS2
002	25,79	26,09	25,90	26,10	26,25	26,13
211	31,08	32,08	31,86	31,92	32,01	32,30
112	32,20	32,41	32,20	-	-	-
300	32,92	33,17	32,90	33,76	33,86	33,90
310	39,81	40,12	39,86	39,61	40,06	39,80
222	46,69	46,95	46,69	46,89	46,93	46,79
213	49,43	49,74	48,16	49,75	50,00	49,76
004	53,21	53,43	53,27	53,41	53,74	53,82

The XRD was not performed for the samples obtained in the meso-OFR due to the limited quantity of sample available. One way of increasing the amount of sample collected is to increase the concentration of the reagents used. It was attempted to increase by 10 times the initial reactants concentration (Appendix F). However, it was found that the formed particles did not correspond to single-phased nano-HAp. It would be necessary to test other concentrations. Another alternative would be to do a continuous-flow process instead of batch.

6.4 Particle size distribution

Regarding the particles produced in the ST, the size distributions in number are unimodal for all the conditions studied (Figure 27 A). The mean particle size of the HAp/SS particles (HAp/SS1 d_{50}: 0,11 µm, HAp/SS2 d_{50}: 0,12 µm) is larger than the mean size of the HAp particles (HAp d_{50}: 0,070 µm). One also observes that the width of the distribution is larger as the SS concentration increases (Table 10). Further, the distribution and particle size obtained for HAp is similar to the ones described in the literature, where HAp particles range in size from 0,050 to 0,23 µm [107], or from 0,040 to 0,11 µm [91]. The size of the HAp particles synthetized is similar to the size of the commercial HAp (d50: 0,058 µm) (Table 10).

For the meso-OFR, the distributions are unimodal, with the exception of the HAp/SS1 particles, whose distribution is biomodal (Figure 27 B). As occurred for the ST, the mean particle size of the particles without SS (HAp d50: 0,40 µm) is smaller when compared to the particles containing SS (HAp/SS1 d50: 0,53 µm, HAp/SS2 d50: 0,54 µm). The broadest distribution corresponds to the HAp particles (Table 10). The mean particle sizes obtained in the meso-OFR are quite large, especially when compared with the literature, where HAp particles with approximately 0,070 µm were synthetized in a meso-OFR [21]. However, SEM and TEM images of the particles shown below (Section 5.5: Figure 32-Figure 34) indicate that the primary particles are at the nanoscale, which probably means that the measured size was of the aggregates.

Regarding the influence of SS, it seems that for both reactors as the concentration of SS increases the mean size of the particles increases (Table 10 and Figure 27 A). This effect is also evidenced in the literature, where the increase of SS concentration was associated with the formation of larger HAp crystals (HAp/1 g/L SS - d_{50}:0,050-0,10 µm, HAp/10 g/L SS - d_{50}:0,30-0,50 µm) [66]. Nano-size HAp exhibits much higher bioactivity than micro-size particles. It provides large interfaces, promoting osteoinductivity and osteoconductivity [114].

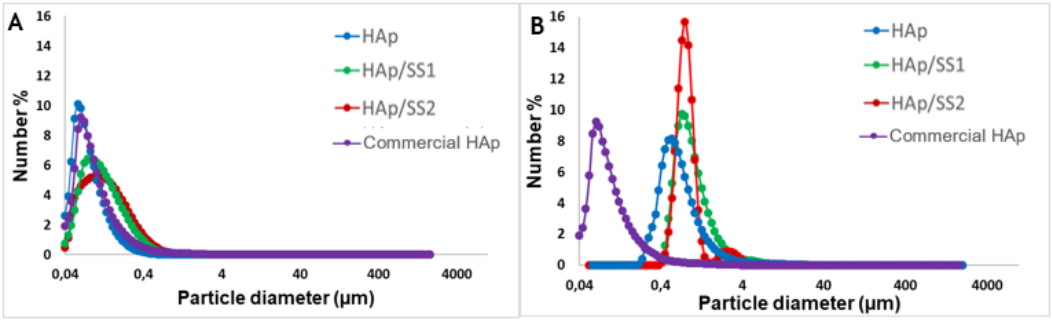

Figure 27 - Particle size distribution in number of the particles produced in the ST (A) and the meso-OFR (B).

In relation to the particle size distributions in volume, in the ST, HAp and HAp/SS1 distributions are multimodal, while HAp/SS2 is unimodal (Figure 28 A). The mean particle size of the HAp/SS particles (HAp/SS1 d_{50}: 161 µm, HAp/SS2 d_{50}: 88,2 µm) is higher when compared to the HAp particles (HAp d_{50}: 8,09 µm) (Table 10).

Regarding the particles obtained in the meso-OFR (Figure 28 B), HAp/SS2 size distribution is biomodal, while for the other conditions the size distributions are multimodal. The mean particle sizes of HAp, HAp/SS1 and HAp/SS2 are 18,6 µm, 48,5 µm and 1,46 µm, respectively. It is noteworthy that for the HAp/SS2 sample the mean size is much lower when compared to the other conditions (Figure 28 and Table 10). This was probably due to some error in the analysis performed.

The aggregates formed in commercial HAp (HAp d_{50}: 0,590 µm) are not as big as the aggregates formed in the particles obtained (Table 10). This may result from the use of some granulometric separation technique.

The presence of several peaks is due to the fact that the particles form aggregates very easily due to their small size [31]. In addition, the suspensions were not subjected to any treatment to separate the aggregates before being analyzed by laser diffraction [89]. Furthermore, due to the limited amount of sample collected in the meso-OFR, the analyzes performed were under low sample conditions. This may have led to the error observed in HAp/SS2.

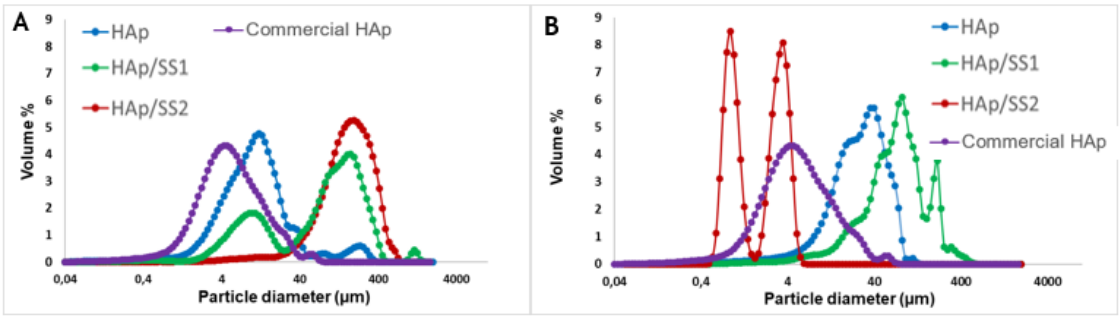

Figure 28 - Particle size distribution in volume of the particles produced in the ST (A) and the meso-OFR (B).

Table 10 - Parameters of the particle size distribution in number of the powders produced in the ST and the meso-OFR at different operating conditions.

Reactor	Condition	d_{10} (μm)	d_{50} (μm)	d_{90} (μm)	span
Number					
ST	HAp	0,046	0,070	0,154	1,54
	HAp/SS1	0,057	0,105	0,255	1,89
	HAp/SS2	0,055	0,116	0,300	2,11
Meso-OFR	HAp	0,240	0,403	0,928	1,71
	HAp/SS1	0,388	0,525	0,764	0,715
	HAp/SS2	0,353	0,538	0,987	1,32
Commercial HAp [86]		0,034	0,058	0,130	1,64
Volume					
ST	HAp	2,27	8,09	19,6	2,14
	HAp/SS1	54,5	161	351	1,85
	HAp/SS2	6,10	88,2	250	2,76
Meso-OFR	HAp	6,44	18,6	39,4	1,77
	HAp/SS1	14,9	48,5	131	2,40
	HAp/SS2	0,495	1,46	2,66	1,48
Commercial HAp [86]		0,150	0,590	2,44	3,88

*d_{10}, 10% of the particles are smaller than this value; d_{50}, 50% of the particles are smaller than this value; d_{90}, 90% of the particles are smaller than this value; span, width of the distribution based on the 10, 50, and 90% quantiles.

6.5 SEM and TEM

Regarding the morphology and size of the prepared particles, SEM and TEM analyses were performed. Aggregated nanoparticles were observed for both reactors (Figure 30 - Figure 34). The obtained nanoparticles adopted a rod-like and plate-like shape, identical to those found in reported results on HAp and HAp/SS nanoparticles [21],[107],[115]. In addition, the HAp particles synthetized are identical to commercial HAp (Figure 29).

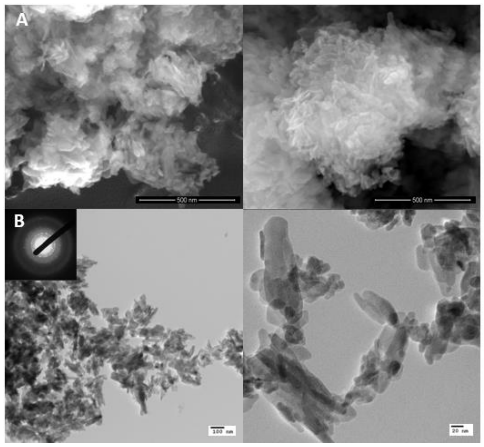

Figure 29 - (A) SEM (B) TEM images of the commercial HAp.

The degree of aggregation of the particles is easily visible in the images of the different microscopy techniques, but the morphology and size of the primary particles is more easily seen in TEM and STEM images since these techniques allow the visualization of nanoscale particles with its higher resolution. While in SEM it is possible to better observe the topography of the aggregated particles, in TEM and STEM it is possible to see the overlapping of what appear to be different planes or structures.

The formation of aggregates was visible in all the samples obtained. However, when compared to the ST (Figure 30 and Figure 31), the meso-OFR particles appear to form higher amount of aggregates (Figure 32 - Figure 34). The aggregation of the primary nanoparticles can explain the large mean size of the particles synthetized in the meso-OFR, observed in the particle size distribution analysis (Figure 27 and Table 10). This tendency to aggregate results from the high surface area to volume ratio of the formed particles, which leads to a high surface tension and consequently to aggregation, as to decrease the surface tension and form more stable particles [116]. According to the obtained images, it is possible to verify that the samples with SS form even more aggregates than the HAp samples. The gelatinous nature of SS may also promote the formation of aggregates [61]. This observation is in agreement with the results obtained in the size distribution in volume, where SS is associated with the formation of more aggregates (Figure 28 and Table 10).The idea was to analyze the sample as it was in the reactor, hence the suspensions analyzed were directly collected from the reactor. However, to reduce the amount of aggregates the suspensions could be subjected to ultrasounds.

Regarding the morphology of the particles, HAp/SS1 (Figure 31-1 and Figure 33) and HAp/SS2 (Figure 31-2 and Figure 34) it appears to include more plate-shaped particles when compared to the HAp samples (Figure 30 and Figure 32). Further, with the increase of SS concentration, more particles seem to take the form of plates. In a study carried out on silk SS it was observed that these protein aggregates forming plate-like particles [117]. In addition, studies on the effect of incorporating amino acids on HAp morphology indicate that Gly (Glycine), Ser(Serine), Asp (Aspartic acid) and Glu (Glutamic acid) lead to the formation of HAp with a flake-like or plate-like shape [118],[119],[120]. SS contains various amino acids, being those present in a higher percentage Ser, Asp and Gly [61]. Beyond aggregation, the presence of plate-shaped structures can explain the results obtained regarding the particle size distribution, as laser diffraction analysis assumes all particles as spherical. HAp morphology can be significantly distinct in different biological tissues, adopting a plate-like structure in bone and rod-like in enamel [121]. Plate-like HAp has a promising shape, because it not only resembles the inorganic phase of bone, but it is also suitable and easy to use in tissue engineering for treatment of bone defects [122], [123]. One of the explanations given for the plate-shaped morphology of HAp and HAp/SS particles is that it is inherited from a precursor OCP or from an amorphous CaP phase. Plate-shape HAp are expected to improve the selectivity about their protein adsorptions [124].

Regarding the crystallinity of the samples, the particles obtained (Figure 30 - Figure 34) appear to be less crystalline when compared to commercial HAp, which presents particles with a more defined structure (Figure 30). This phenomenon, also verified in XRD, FTIR and SAED, may be due to the use of different methods for HAp synthesis [125]. With the increase of SS concentration, the crystallinity of the samples appears to decrease. Through the electron diffraction patterns, it is demonstrated that the commercial HAp is a polycrystalline structure (Figure 30 B), since the ring pattern consist of small spots and a defined ring. As for the HAp/SS samples of the ST, it is possible to see that the particles formed are poor crystalline, since the

electron patterns show diffuse rings. The size of the rings decreased with increasing SS, which suggested that the crystallinity decreased (Figure 31) [104]. Moreover, for HAp/SS1 it is possible to identify the existence of small bright points in addition to the central ring, whereas in HAp/SS2 these points no longer occur. A previous work suggested that there was no perceptible change in the crystallinity of HAp/SS particles with the change in SS concentration, but that the HAp/SS particles had lower crystallinity than the HAp particles [66]. The presence of the characteristic SS amino acids, has also been associated with decreased crystallinity [118]. This may be interesting for further interaction with cells, since they present greater bioactivity. Less crystalline materials have been found to be more resorbable and there is evidence to suggest that they may be more beneficial for early bone ingrowth than particles with high crystallinity [126]. In addition, the presence of SS, which is a bioactive molecule, gives rise to an improved biological response in terms of cell proliferation [127].

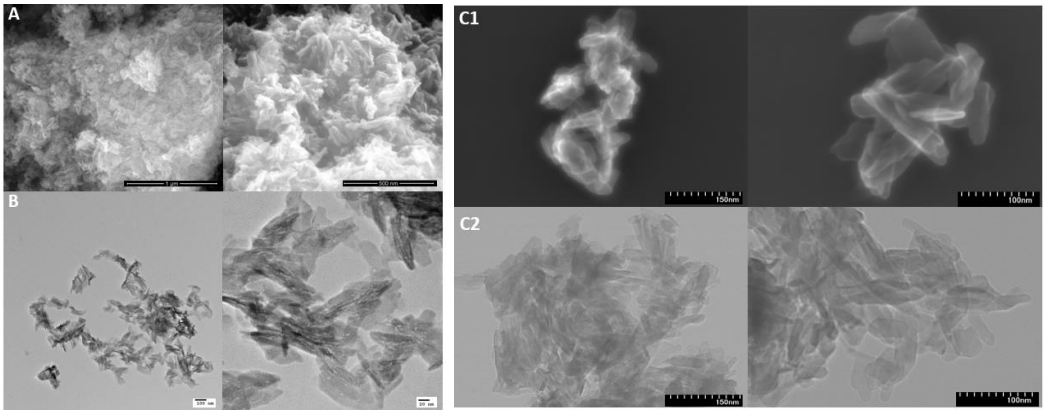

Figure 30 - (A) SEM, (B) TEM and (C) STEM images of the HAp particles obtained in the ST.

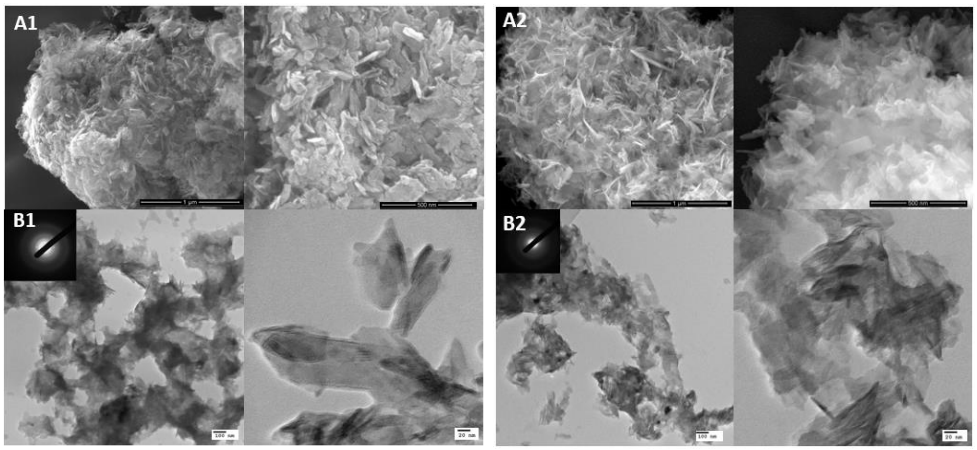

Figure 31 - (A1) HAp/SS1 SEM; (B1) HAp/SS1 TEM; (A2) HAp/SS2 SEM; (B2) HAp/SS2 TEM images of HAp/SS particles obtained in the ST.

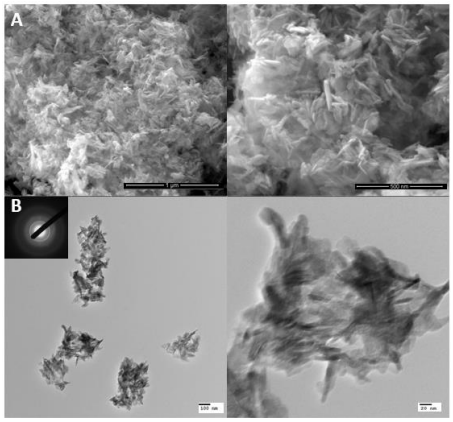

Figure 32 - (A) SEM and (B) TEM images of HAp particles obtained in the meso-OFR.

As already discussed in section 6.1, HAp is the most thermodynamically stable CaP in the used conditions. However, for the HAp/SS1 obtained in the meso-OFR, in addition to the typical nano-HAp particles, the formation of the kinetically most favored phases can be observed [39],[107]. The visualized structure in Figure 33 is in the μm order and has a plate-like shape. According to these features, the CaP may be OCP [128],[129], but further analysis is needed to confirm this observation. This CaP is known to be a precursor during the bone mineralization process and has been successfully applied as a coating of metal prostheses, leading to the precipitation of several layers of carbonated amorphous CaP in the support structure [130]. Due to its potential, the presence of OCP may promote the biological response of the developed nanocomposites.

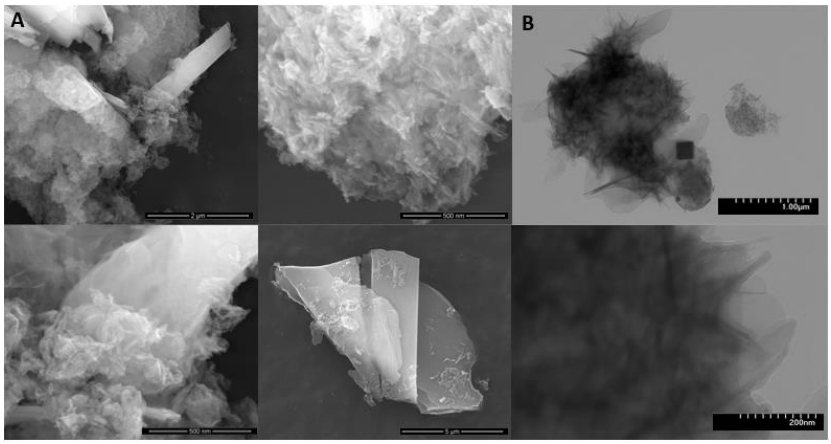

Figure 33 - (A) SEM and (B) STEM images of HAp/SS1 particles obtained in the meso-OFR.

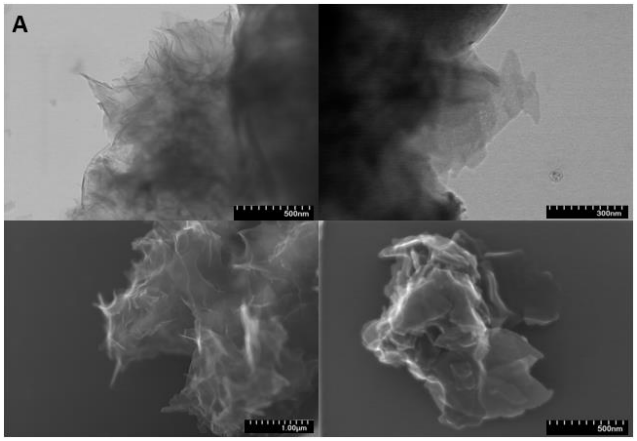

Figure 34 - (A) SEM and (B) STEM images of HAp/SS2 particles obtained in the meso-OFR.

The visualization of the HAp/SS particles formed in the meso-OFR was difficult due to the presence of water in the samples. Besides the water that remains between the particles due to centrifugation, the water can also be attributed to the water absorption capacity of SS [56]. It was not possible to obtain the images of the different microscopes used for these samples.

SEM image of HAp/SS2 showed sodium chloride salts (equation 5.1), which were formed when the sample was subjected to vacuum, avoiding the visualization of the HAp/SS nanoparticles. The presence of salts was notorious in the meso-OFR, having been identified for all HAp/SS conditions. This can be explained by the collecting method of the samples, since no filtration of the suspension collected from the reactor was performed.

SEM/EDS was performed for the samples obtained in the ST (Figure 35), confirming the formation of CaP, since for the three conditions studied the main elements detected are Ca and P. The use of the carbon tape to attach the sample to the carrier used may contribute to the presence of C [131]. The identification of O may be due to its existence in the HAp structure ($Ca_{10}(PO_4)_6(OH)_2$) [132],[115]. Through EDS analysis it was also possible to identify the presence of N for the experimental condition with higher SS concentration, and an increase of intensity of C, which indicates the presence of SS (Figure 35 C) [133]. In addition, for all the ST samples, the intensity of the peaks relative to Ca is lower than those of P. Although the analysis is qualitative and depends on several factors, this is in agreement with the identification of OHAp (Figure 35).

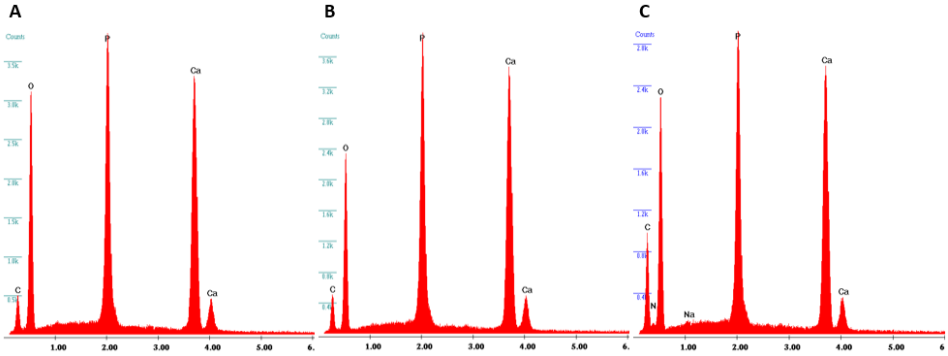

Figure 35 - EDS of the samples obtained in the ST (A) HAp (B) HAp/SS1 and (C) HAp/SS2.

The elemental analysis of HAp and HAp/SS2 samples of the meso-OFR was made through STEM/EDS, confirming the presence of Ca and P (Figure 36). The presence of Na and Cl was also detected, representing the presence of salt in these samples. The presence of Cu can be attributed to the support used for the analysis. In contrast to the ST samples, Ca peaks have higher intensity than P. EDS is a qualitative technique, and although it does not allow to confirm the type of HAp and HAp/SS particles synthesized, it gives relevant information (Figure 36).

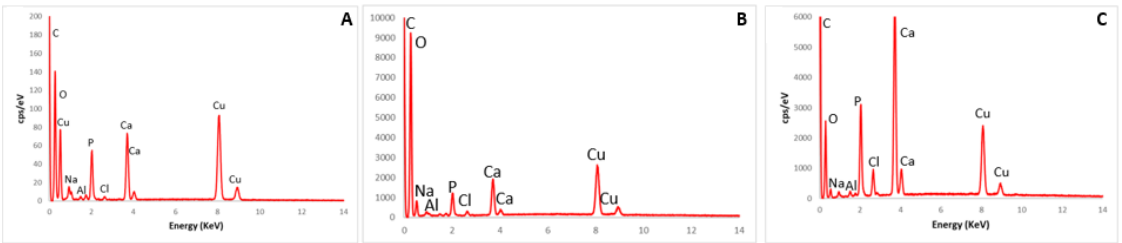

Figure 36 - EDS of the samples obtained in the meso-OFR (A) HAp; (B) HAp/SS1; (B) HAp/SS2.

6.6 - Comparison of the HAp particles obtained with those of the NETMIX reactor

HAp exhibits a high degree of chemical and physical variability, depending on the final application. Comparing the particles synthetized, with the HAp particles obtained in the NETMIX, it was found that these particles have different characteristics (Table 11).

HAp with high crystallinity, purity and stoichiometry is widely used in applications where the main purpose is to have a biocompatible material, similar to the inorganic phase of the bone, for bone grafts and coated implants. This applies to the particles obtained in the NETmix reactor and concerns the replacement and repair of bone tissue [83]. On the other hand non-crystalline, low purity and non-stoichiometric HAp, similar to the particles studied, is used in applications where the goal is to promote cell differentiation and proliferation, such as bone fills and scaffolds. This is related to the regeneration of bone tissues [35],[3].

Furthermore, the methodology used in this work is simpler compared to that used in Fluidinova.S.A. In the NETmix reactor, HAp is produced by wet chemical precipitation method at room temperature. An alkaline solution is used to control the solution pH between 9 and 12. The suspensions are centrifuged, washed and dried at 70 ºC to produce HAp dry powder [91]. In the present study, the chosen conditions came closer to the physiological conditions of the human body (T=37ºC and pH between 6 and 8) and only strictly necessary reagents were used.

Table 11 - Characteristics of the obtained particles and the particles obtained in the NETMIX reactor [83],[91],[106].

Characteristics	HAp obtained	HAp obtained in the NETmix
Crystallinity	Low	High
Morphology	Rod-like and plate-like shape	Rod-like shaped
Size (μm)*	d_{50} HAp: 0,07; d_{50} HAp/SS1: 0,11; d_{50} HAp/SS2: 0,12	0,06
Stoichiometry	Non- stoichiometric	Stoichiometric
Purity	Presence of other CaP (OCP).	High phase purity

* Only the mean particle sizes obtained in the ST were considered, since the mean particle size obtained in the meso-OFR was attributed to aggregation.

Chapter 7

Conclusions

7.1 Objectives achieved and main conclusions

Several studies have focused on the formation of nanocomposite materials, namely the conjugation of hydroxyapatite (HAp) with an organic matrix in order to obtain materials with improved properties. Sericin (SS) has been of interest because of expected improved biological response in terms of cell adhesion, cell infiltration and vascularization, as recently reported. However, the influence of SS on HAp particles is still very little discussed in the literature.

In the present work, HAp/SS nanocomposites were successfully synthesized using a ST (stirred tank batch reactor) and a meso-OFR (meso oscillatory flow reactor) through a simple wet chemical precipitation method, under near physiological conditions of pH and temperature. The precipitation process in both reactors was characterized by monitoring the pH profiles during the experiments and by characterization of the particles obtained. Despite the differences between the two reactors, namely the hydrodynamic conditions and sample collection methods, the comparison of these two reactors was important to evaluate their performance in the synthesis of the HAp/SS particles.

The design of a simple and inexpensive method for the synthesis of the studied nanocomposites was one of the achieved objectives of this work. The technique used for the extraction of SS (heat extraction) was also chosen because it does not require chemicals or introduce byproducts. Also, no additional steps are needed. The experimental conditions were chosen so as to resemble the physiological conditions of the human organism. These were easy to maintain and no extreme environment was needed. Therefore, the scalability of the herein proposed methodology is highly attainable, which facilitates its industrialization.

The pH profiles allowed for the monitorization of the precipitation process chemistry over time. In the ST the pH profiles showed the presence of six stages for all the conditions studied. For the meso-OFR, the formation of different stages did not occur, which may mean that there is no formation of intermediate CaP phases. The formation of the HAp/SS nanocomposites is therefore achieved in less time, being approximately 4 times faster. Accordingly, besides being

more efficient in the synthesis of HAp/SS nanocomposites, the meso-OFR reduces reagent requirements and waste. This is particularly useful in preliminary studies of a given process, but also when taking the technology to mass production.

As to the characterization of the particles, FTIR analysis evidenced the presence of most of the bands attributed to HAp. For the HAp/SS particles, in addition to the presence of HAp, it was also possible to detect the presence of amides, which are characteristic of SS. These peaks were more easily identified for the experimental condition with higher concentration of SS. The same occurred for the EDS analysis, where it was possible to identify the presence of N for HAp/SS2 obtained in the ST.

The formation of nano-HAp with poor crystallinity in the ST was confirmed by XRD. In the meso-OFR, the low crystallinity of the samples was mainly visible through SAED. The synthesized particles are less crystalline than the commercial HAp, which was also verified through electron diffraction patterns. In addition, the increase in SS concentration is associated with lower crystallinity, which may be advantageous in the interaction with bone cells, in an *in vivo* scenario.

Through the particle size distribution in number it was found that with the increase in SS concentration an increase in the mean particle size occurs. The particle size distribution in volume indicated the presence of several aggregates. The aggregation was especially high in the meso-OFR, where the particle sizes obtained were superior to those that would be expected.

SEM and TEM images show that the primary particles obtained in both reactors are similar in size (nm) and morphology. From these observations, it was possible to realize that all the nanoparticles adopt a rod-like and plate-like shape. Aggregation was also visible for all the conditions studied which is consistent with the particle distribution results. The features of the particles synthetized correspond to the characteristics described for HAp. Furthermore, an increase in SS concentration was associated with the formation of more plate-shaped particles. This plate-like morphology, being similar to biological bone, is used in several applications of tissue engineering.

In addition, the EDS for all the conditions in the ST have Ca peaks with a lower intensity than for P, which may suggest that the formed HAp is deficient in calcium. However, in the meso-OFR, this was not verified.

The synthesized HAp particles and HAp/SS nanocomposites also have economic potential, at least in Portugal, since there is no company that manufactures and distributes this material with specific characteristics in bone regeneration applications.

7.2 Limitations and Solutions

The main limitation of this work was the amount of sample obtained from the meso-OFR. In view of this, the method utilized to collect the sample had to be different from that of the ST. The particles obtained in the meso-OFR were collected by centrifugation, and thus the quantity of mother liquor that remains is higher. Furthermore, SS has a high water holding capacity. This interfered with some characterization techniques, such as FTIR, SEM and TEM. In FTIR, it was more complicated to identify amide I, since its peak is very close to a peak attributed to adsorbed water. For some HAp/SS particles, it was not possible to obtain SEM or TEM images. To increase the amount of sample collected it would be necessary to increase the initial reagent concentration or pass the precipitation process to continuous.

In addition, the formation of aggregates made it difficult to analyze the particle size distributions and visualize the primary particles by microscopy. This impaired the evaluation of the obtained nanocomposites in terms of size distribution, size and morphology. To reduce aggregation, it would be necessary to subject the obtained suspensions to ultrasounds.

7.3 Future work and perspectives

As future work, one intends to perform the missing characterization techniques, namely the XRD for the meso-OFR, as well as to perform additional characterization techniques such as to determine the Ca/P molar ratio, in order to confirm that the particles obtained are calcium deficient. The next step will be to study the interaction of the HAp/SS nanoparticles with bone cells. These nanocomposites could be of interest as bone filling and stimulation of *in vitro* regeneration.

In summary, the work developed presents a simple and effective method for the synthesis of HAp/SS nanocomposites in a meso-OFR (Table 12). This reactor allowed the synthesis of the desired nanocomposites in considerably less time.

Table 12 - Summary of the main conclusions of the work developed.

Objectives met	-Elaboration of a simple method to synthetize HAp/SS nanocomposites with less additional chemical compounds and experimental steps; - Performance comparison of a ST and a meso-OFR; - Characterization of HAp/SS nanocomposites obtained; - Better performance of the meso-OFR when compared to the ST to synthetize HAp/SS; - Evaluation of the effect of SS concentration on HAp size and morphology.
Limitations/ Solution	- Small amount of sample collected from the meso-OFR/ Increase the concentration of the reagents used; Pass the process to continuous; - Formation of aggregates / thermal treatment or granulometric separation;
Future perspectives	- Repetition of the characterization techniques for the missing conditions; - Determination of the Ca/P molar ratio; - Evaluation of the behavior of bone tissue cells in the presence of the HAp/SS nanocomposites.

References

[1] M. Martins, "Desenvolvimento de hidrogéis à base de quitosano / fosfatos de cálcio para aplicações ortopédicas," Tese de Mestrado na Faculdade de Ciência e Tecnologia da Universidade Nova de Lisboa, 2012.

[2] F. Leahy, D. Miranda, L. Duarte, A. Consolaro, and C. Francischone, *Evidências científicas em estética e osseointegração*, 1ª Edição. Associação de Osseointegração do Nordeste, 2013.

[3] K. Lin and J. Chang, *Hydroxyapatite (HAp) for Biomedical Applications*, vol. 4214, no. 8. Woodhead Publishing, 2015.

[4] H. P. Zhang, X. Y. Wang, S. J. Min, M. Mandal, M. Y. Yang, and L. J. Zhu, "Hydroxyapatite/sericin composite film prepared through mineralization of flexible ethanol-treated sericin film with simulated body fluids," *Ceram. Int.*, vol. 40, no. 1 Part A, pp. 985–991, 2014.

[5] M. A. Cunha, "Síntese e caracterização de Hidroxiapatita nanoestruturada obtidos por aspersão de solução em chama," Tese de Mestrado na Escola de Engenharia da Universidade Federal do Rio Grande Sul, 2010.

[6] A. Takeuchi, C. Ohtsuki, T. Miyazaki, and M. Kamitakahara, "Heterogeneous nucleation of hydroxyapatite on protein: structural effect of silk sericin," *J. R. Soc. Interface*, vol. 2, no. 4, pp. 373–8, 2005.

[7] D. A. Wahl and J. T. Czernuszka, "Collagen-hydroxyapatite composites for hard tissue repair," *Eur. Cells Mater.*, vol. 11, no. 3, pp. 43–56, 2006.

[8] L. Pighinelli and M. Kucharska, "Chitosan-hydroxyapatite composites," *Carbohydr. Polym.*, vol. 93, no. 1, pp. 256–262, 2013.

[9] L. Liu *et al.*, "Preparation and characterization of nano-hydroxyapatite/silk fibroin porous scaffolds," *J. Biomater. Sci. Polym. Ed.*, vol. 19, no. 3, pp. 325–338, 2008.

[10] X. Wang, X. Wang, Y. Tan, B. Zhang, Z. Gu, and X. Li, "Synthesis and evaluation of collagen-chitosan- hydroxyapatite nanocomposites for bone grafting," *J. Biomed. Mater. Res. - Part A*, vol. 89, no. 4, pp. 1079–1087, 2009.

[11] L. Chen, J. Hu, J. Ran, X. Shen, and H. Tong, "Preparation and evaluation of collagen-silk fibroin/hydroxyapatite nanocomposites for bone tissue engineering," *Int. J. Biol. Macromol.*, vol. 65, no. 4, pp. 1–7, 2014.

[12] T. Gong, J. Xie, J. Liao, T. Zhang, S. Lin, and Y. Lin, "Nanomaterials and bone regeneration," *Bone Res.*, vol. 3, no. 8, p. 15029, 2015.

[13] A. C. Guastaldi and A. H. Aparecida, "Fosfatos de cálcio de interesse biológico:Importância como biomaterias, propriedades e métodos de obtenção de recobrimentos," *Quim. Nova*, vol. 33, no. 6, pp. 1352–1358, 2010.

[14] L. Lamboni, M. Gauthier, G. Yang, and Q. Wang, "Silk sericin: A versatile material for tissue engineering and drug delivery," *Biotechnol. Adv.*, vol. 33, no. 8, pp. 1855–1867, 2015.

[15] R. Kunz, R. Brancalhão, L. Ribeiro, and M. Natali, "Silkworm Sericin: Properties and Biomedical Applications," *Biomed Res. Int.*, vol. 2016, pp. 1–19, 2016.

[16] R. Lindenbergh, "Extraction and characterization of sericin and its immobilization on hydroxyapatite nanoparticles for tissue engineering applications," *Int. J. ChemTech Res.*, vol. 7, no. 5, pp. 2117–2124, 2010.

[17] A. Pires, A. Bierhalz, and A. Moraes, "Biomateriais: Tipos, aplicações e mercados," *Quim. Nova*, vol. 38, no. 7, pp. 957–971, 2015.

[18] L. Chen, J. Hu, J. Ran, X. Shen, and H. Tong, "A novel nanocomposite for bone tissue engineering based on chitosan–silk sericin/hydroxyapatite: biomimetic synthesis and its cytocompatibility," *R. Soc. Chem.*, vol. 5, no. 69, pp. 56410–56422, 2015.

[19] F. Castro, A. Ferreira, F. Rocha, A. Vicente, and J. A. Teixeira, "Continuous-Flow Precipitation of Hydroxyapatite at 37 °C in a Meso Oscillatory Flow Reactor," *AIChE J.*, vol. 59, no. 12, pp. 4483–4493, 2013.

[20] A. V. A. Ferreira, F. Rocha, J.A. Teixeira, “Apparatus for mixing improvement based on oscillatory flow reactors provided with smooth periodic constrictions. Int. Patent WO 2015/056156 A1.,” PCT/IB2014/065273, 2014.

[21] F. Castro, A. Ferreira, F. Rocha, A. Vicente, and J. Teixeira, “Precipitation of Hydroxyapatite at 37º C in a Meso Oscillatory Flow Reactor Operated in Batch at Constant Power Density,” *AIChE J.*, vol. 7, no. Part 1, pp. 405–410, 2014.

[22] P. Moraes, “Estudo comparativo da membrana e do hidrogel de celulose bacteriana com colágeno em dorso de ratos,” Tese de Mestrado na Escola de Engenharia da Universidade de São Carlos, 2013.

[23] H. Reza Rezaie, L. Bakhtiari, and A. Öchsner, *Biomaterials and Their Applications*. Springer, 2015.

[24] P. Parida, A. Behera, and S. C. Mishra, “Classification of Biomaterials used in Medicine,” *Int. J. Adv. Appl. Sci.*, vol. 1, no. 3, pp. 125–129, 2012.

[25] P. S. P. De Carvalho, A. L. Rosa, A. Paula, F. Bassi, L. Antonio, and V. Dias, “Biomateriais aplicados a Implantodontia,” *Rev. Implant.*, vol. 7, pp. 56–65, 2010.

[26] A. Afonso, “Interacção entre Biomateriais e Tecido Ósseo,” Tese de Doutoramento na Faculdade Dentária da Universidade de Porto, 1998.

[27] L. L. Hench, “Bioceramics : From Concept to Clinic,” *Am. Ceram. Soc. Bull.*, vol. 72, no. 4, pp. 93–98, 1993.

[28] F. Baino, G. Novajra, and C. Vitale-Brovarone, “Bioceramics and Scaffolds: A Winning Combination for Tissue Engineering,” *Front. Bioeng. Biotechnol.*, vol. 3, no. 12, pp. 1–17, 2015.

[29] R.L.Reis and S.Weiner, *Learning from Nature How to Design new Implantable biomaterials*. Kluwer Academic, 2005.

[30] S. J. Kalita, A. Bhardwaj, and H. A. Bhatt, “Nanocrystalline calcium phosphate ceramics in biomedical engineering,” *Mater. Sci. Eng. C*, vol. 27, no. 3, pp. 441–449, 2007.

[31] F. Castro, “Process Intensification for the production of hydroxyapatite nanoparticles,” Tese de Doutoramento na Escola de Engenharia da Universidade do Minho, 2013.

[32] A. H. Aparecida *et al.*, “Estudo da influência dos iões K+,Mg2+,So2-4 e Co2-3 na cristalização biomimétrica de fosfato de cálcio amorfo (ACP) e conversão a fofato octacálcico (OCP),” vol. 30, no. 4, pp. 892–896, 2007.

[33] M. P. Ferraz, F. J. Monteiro, and C. M. Manuel, “Hydroxyapatite nanoparticles : A review of preparation methodologies,” *J. Appl. Biomater.*, vol. 2, no. 2, pp. 74–80, 2004.

[34] A. Szcześ, L. Hołysz, and E. Chibowski, “Synthesis of hydroxyapatite for biomedical applications,” *Adv. Colloid Interface Sci.*, vol. 249, no. 4, pp. 321–330, 2017.

[35] A. C. F. M. Costa, M. G. Lima, L. H. M. A. Lima, V. V Cordeiro, and K. M. S. Viana, “Hidroxiapatita: Obtenção, caracterização e aplicações,” *Rev. Eletrônica Mater. e Process.*, vol. 3, no. 11, pp. 29–38, 2009.

[36] R. Citfcioglu, “The Preparation and characterization of hydroxyapatite bioceramic implant material,” Master degree inn Science in Izmir Institute of Technology, 2000.

[37] J. W. Mullin, *Crystallization*, 4th Editio. Oxford: Reed Educational and professional publishing Ltd, 2001.

[38] G. Ma and X. Y. Liu, “Hydroxyapatite: Hexagonal or monoclinic?,” *Cryst. Growth Des.*, vol. 9, no. 7, pp. 2991–2994, 2009.

[39] J.C.Elliot, *Struture and Chemistry of the Apatites and Other Calcium Orthophosphates*, 1st Editio. Elsevier, 1994.

[40] S. Sunarintyas and W. Siswomihardjo, “The effect of sericin application over hydroxyapatite surface on osteoblast cells proliferation,” *Proc. - Int. Conf. Instrumentation, Commun. Inf. Technol. Biomed. Eng.*, no. 11, pp. 145–149, 2011.

[41] L. Wang and G. H. Nancollas, “Calcium orthophosphates: Crystallization and Dissolution,” *Chem. Rev.*, vol. 108, no. 11, pp. 4628–4669, 2008.

[42] S. Marković, L. Veselinović, M. J. Lukić, and L. Karanović, “Synthetical bone-like and biological hydroxyapatites: a comparative study of crystal structure and morphology,” *Biomedical Materials*, vol. 6, no. 4, p. 45005, 2011.

[43] T. Leventouri, “Synthetic and biological hydroxyapatites: Crystal structure questions,” *Biomaterials*, vol. 27, no. 18, pp. 3339–3342, 2006.

[44] A. Siddharthan, S. Seshadri, and T. Kumar, “Rapid Synthesis of Calcium Deficient Hydroxyapatite Nanoparticles by Microwave Irradiation .,” *Trends Biomater. Artif. Organs*, vol.

18, no. 2, pp. 110–113, 2005.
[45] M. Sadat-Shojai, M. T. Khorasani, E. Dinpanah-Khoshdargi, and A. Jamshidi, “Development of high strength hydroxyapatite by solid-state-sintering process,” *Acta Biomater.*, vol. 9, no. 8, pp. 7591–7621, 2013.
[46] V. Silva, R. Domingues, and F. Lameiras, “Microstructural and mechanical study of zirconia-hydroxyapatite,” *Compos. Sci. Technol.*, vol. 61, no. 2, pp. 301–310, 2001.
[47] J. Dusza, M. Hnatko, and S. Republic, “Densification route and mechanical properties of Si3N4–bioglass biocomposites,” *Biomaterials*, vol. 3, pp. 350–353, 2005.
[48] Q. Chen, C. Zhu, and G. A. Thouas, “Progress and challenges in biomaterials used for bone tissue engineering: bioactive glasses and elastomeric composites,” *Prog. Biomater.*, vol. 1, no. 1, pp. 1–22, 2012.
[49] B. Rocha *et al.*, “Stress distribution on maxillary central incisor under similar traumatic situations with different loading forces : a 3-D finite element analysis,” *Arq Odontol, Belo Horiz.*, vol. 49, no. 2, pp. 52–59, 2013.
[50] M. Giannini, C. J. Soares, and R. M. De Carvalho, “Ultimate tensile strength of tooth structures,” *Dent. Mater.*, vol. 20, no. 4, pp. 322–329, 2004.
[51] J. Ivancik and D. D. Arola, “The importance of microstructural variations on the fracture toughness of human dentin,” *Biomaterials*, vol. 34, no. 4, pp. 864–874, 2013.
[52] M. Á. Garrido, I. Giráldez, L. Ceballos, and J. Rodríguez, “On the possibility of estimating the fracture toughness of enamel,” *Dent. Mater.*, vol. 30, no. 11, pp. 1224–1233, 2014.
[53] L. Peixoto, “Preparação de compósitos e nanocompósitos poliméricos in situ,” Tese de Doutoramento no Instituto Alberto Luiz Coimbra na Universidade Federal do Rio de Janeiro, 2012.
[54] P. Aramwit, S. Kanokpanont, T. Nakpheng, and T. Srichana, “The effect of sericin from various extraction methods on cell viability and collagen production,” *Int. J. Mol. Sci.*, vol. 11, no. 5, pp. 2200–2211, 2010.
[55] A. U. U. Ude, R. A. A. Eshkoor, R. Zulkifili, A. K. K. Ariffin, A. W. W. Dzuraidah, and C. H. H. Azhari, “Bombyx mori silk fibre and its composite: A review of contemporary developments,” *Mater. Des.*, vol. 57, no. 12, pp. 298–305, 2014.
[56] P. Robinson and R. Kwong, “The silk proteins, sericin and fibroin in silkworm, Bombyx mori Linn., - a review,” *Casp. J. Environ. Sci.*, vol. 25, no. 4, pp. 77–84, 2006.
[57] M. L. Gimenes, V. R. Silva, M. G. a. Vieira, M. G. C. Silva, and A. P. Scheer, “High Molecular Sericin from Bombyx mori Cocoons: Extraction and Recovering by Ultrafiltration,” *Int. J. Chem. Eng. Appl.*, vol. 5, no. 3, pp. 266–271, 2014.
[58] Y. Q. Zhang, “Applications of natural silk protein sericin in biomaterials,” *Biotechnol. Adv.*, vol. 20, no. 2, pp. 91–100, 2002.
[59] S. C. Kundu, B. C. Dash, R. Dash, and D. L. Kaplan, “Natural protective glue protein, sericin bioengineered by silkworms: Potential for biomedical and biotechnological applications,” *Prog. Polym. Sci.*, vol. 33, no. 10, pp. 998–1012, 2008.
[60] M. N. Padamwar and A. P. Pawar, “Silk sericin and its application : A review,” *J. Sci. Ind. Res. (India).*, vol. 63, no. 10, pp. 323–329, 2004.
[61] J. A. Barajas-Gamboa, A. M. Serpa-Guerra, A. Restrepo-Osorio, and C. Álvarez-López, “Sericin applications: a globular silk protein,” *Ing. y Compet.*, vol. 18, no. 2, pp. 193–206, 2016.
[62] S. K. Rajput and M. Kumar Singh, “Sericin – A unique biomaterial,” *IOSR J. Polym. Text. Eng.*, vol. 2, no. 3, pp. 2348–181, 2015.
[63] L. Lamboni, Y. Li, J. Liu, and G. Yang, “Silk Sericin-Functionalized Bacterial Cellulose as a Potential Wound-Healing Biomaterial,” *Biomacromolecules*, vol. 17, p. 3076−3084, 2016.
[64] S. Ghosh, R. S. Rao, K. S. Nambiar, V. C. Haragannavar, D. Augustine, and S. V Sowmya, “Sericin, a dietary additive: mini review,” *J. Med. Radiol. Pathol. Surg.*, vol. 4, pp. 13–17, 2017.
[65] J. H. Lee, D. W. Song, Y. H. Park, and I. C. Um, “Effect of residual sericin on the structural characteristics and properties of regenerated silk films,” *Int. J. Biol. Macromol.*, vol. 89, pp. 273–278, 2016.
[66] Y. Cai, J. Jin, D. Mei, N. Xia, and J. Yao, “Effect of silk sericin on assembly of hydroxyapatite nanocrystals into enamel prism-like structure,” *J. Mater. Chem.*, vol. 19, no. 32, p. 5751, 2009.
[67] J. P. M. Inacio and T. R. Brazil, “Biomineralização in vitro de compósitos de Hidroxiapatita e nanotubos de carbono utilizando fluido corporal simulado,” Tese de Mestrado no Instituto de Pesquisa e Desenvolvimento da Universidade do Vale do Paraíba, 2013.

[68] K. Lima, "Estudo da cristalização e elaboração de prática didática em cristalizador batelada agitado," Tese de Mestrado no Campus avançado de Poços de Caldas na Universidade Federal de Alfenas, 2014.
[69] A. Mersmann, *Crystallization Technology Handbook*. New York: CRC Press, 1995.
[70] E. C. M.Giulietti, M.M.Seckler, S.Derenzo, M.I.Ré, "Industrial Crystallization and precipitation from solutions: state of the technique," *Brazilian J. Chem. Eng.*, vol. 18, no. 4, pp. 1678–4383, 2001.
[71] P. Cruz, "Aplicação de um novo reator de fluxo oscilatório no controlo da qualidade e tamanho dos cristais de paracetamol," Tese de Mestrado na Faculdade de Engenharia da Universidade do Porto, 2015.
[72] I. R. Krauss, A. Merlino, A. Vergara, and F. Sica, "An overview of biological macromolecule crystallization," *Int. J. Mol. Sci.*, vol. 14, no. 6, pp. 11643–11691, 2013.
[73] A. Ferreira, "Caracterização fenomenológica dos processos de transferência de impurezas para os cristais," Tese de Doutoramento na Faculdade de Engenharia da Universidade do Porto, 2008.
[74] A. S. Myerson, *Handbook of Industrial Crystallization*. Butterworth-Heinemann, 2002.
[75] N. Y. Mostafa and P. W. Brown, "Computer simulation of stoichiometric hydroxyapatite: Structure and substitutions," *J. Phys. Chem. Solids*, vol. 68, no. 3, pp. 431–437, 2007.
[76] P. Cubillas and M. W. Anderson, *Synthesis Mechanism: Crystal Growth and Nucleation*. WILEY-VCH Verlag GmbH & Co. KGaA, Weinheim, 2010.
[77] J. G. Otakar Sohnel, *Precipitation*. Butterworth-Heinemann, 1992.
[78] M. Kind, "Colloidal aspects of precipitation processes," *Chem. Eng. Sci.*, vol. 57, no. 20, pp. 4287–4293, 2002.
[79] O. Söhnel and J. Garside, *Precipitation: Basic Principles and Industrial Applications*. Butterworth-Heinemann, 1992.
[80] M. J. J. M. van Kemenade and P. L. de Bruyn, "A kinetic study of precipitation from supersaturated calcium phosphate solutions," *J. Colloid Interface Sci.*, vol. 118, no. 2, pp. 564–585, 1987.
[81] M. Wei, A. J. Ruys, B. K. Milthorpe, and C. C. Sorrell, "Precipitation of hydroxyapatite nanoparticles: Effects of precipitation method on electrophoretic deposition," *J. Mater. Sci. Mater. Med.*, vol. 16, no. 4, pp. 319–324, 2005.
[82] J. F. Gomes, C. C. Granadeiro, M. a Silva, M. Hoyos, R. Silva, and T. Vieira, "An Investigation of the Synthesis Parameters of the Reaction of Hydroxyapatite Precipitation in Aqueous Media," *Int. J. Chem. React. Eng.*, vol. 6, no. 1, pp. 1–15, 2008.
[83] V. Silva, P. Quadros, P. Laranjeira, M. Dias, and J. Lopes, "A novel continuous industrial process for producing hydroxyapatite nanoparticles," *J. Dispers. Sci. Technol.*, vol. 29, no. 4, pp. 542–547, 2008.
[84] E. M. Davis and R. J. Davis, *Fundamentals of Chemical Reaction Engineering*, vol. 43, no. 9. McGraw-Hill Education, 2003.
[85] J. Chen and C. Zheng, "Interaction of macro-and micromixing on particle size distribution in reactive precipitation," *Chem. Eng. Sci.*, vol. 51, no. 10, pp. 1957–1966, 1996.
[86] F. Castro *et al.*, "Process intensification and optimization for hydroxyapatite nanoparticles production," *Chem. Eng. Sci.*, vol. 100, pp. 352–359, 2013.
[87] L. G. and Y.-T. A. Qing Yang, Jie-Xin Wang, Lei Shao, Qi-An Wang, Fen Guo, Jian-Feng Chen, "High Throughput Methodology for Continuous Preparation of Hydroxyapatite Nanoparticles in a Microporous Tube-in-Tube Microchannel Reactor," *Ind. Eng. Chem. Res.*, vol. 49, no. 1, pp. 140–147, 2010.
[88] R. Zauner, "Scale-Up of Precipitation Processes," PhD Thesis at Ramsay Memorial Laboratory of Chemical Engineering at University of London, 1994.
[89] F. Castro *et al.*, "Continuous-flow precipitation of hydroxyapatite in ultrasonic microsystems," *Chem. Eng. J.*, vol. 215–216, pp. 979–987, 2013.
[90] C. M. Fonte, M. E. Leblebici, M. M. Dias, and J. C. B. Lopes, "The NETmix reactor: Pressure drop measurements and 3D CFD modeling," *Chem. Eng. Res. Des.*, vol. 91, no. 11, pp. 2250–2258, 2013.
[91] P. J. Gomes, V. M. T. M. Silva, P. a. Quadros, M. M. Dias, and J. C. B. Lopes, "A Highly Reproducible Continuous Process for Hydroxyapatite Nanoparticles Synthesis," *J. Nanosci. Nanotechnol.*, vol. 9, no. 6, pp. 3387–3395, 2009.
[92] H. Schlichting and K. Gersten, *Boundary-Layer Theory*. Springer, 1951.

[93] “Reynolds Number,” *Nuclear Power*. [Online]. Available: http://www.nuclear-power.net/nuclear-engineering/fluid-dynamics/reynolds-number/. [Accessed: 05-Dec-2017].
[94] Q. Yang *et al.*, “High throughput methodology for continuous preparation of hydroxyapatite nanoparticles in a microporous tube-in-tube microchannel reactor,” *Ind. Eng. Chem. Res.*, vol. 49, no. 1, pp. 140–147, 2010.
[95] N. M. Reis, “Novel Oscillatory Flow Reactors for Biotechnological Applications,” Tese de Doutoramento na Escola de Engenharia da Universidade do Minho, 2006.
[96] M. S. R. Abbott, A. P. Harvey, G. V. Perez, and M. K. Theodorou, “Biological processing in oscillatory baffled reactors: operation, advantages and potential,” *Interface Focus*, vol. 3, no. 1, pp. 1–13, 2012.
[97] A. W. Fitch, H. Jian, and X. Ni, “An investigation of the effect of viscosity on mixing in an oscillatory baffled column using digital particle image velocimetry and computational fluid dynamics simulation,” *Chem. Eng. J.*, vol. 112, no. 1–3, pp. 197–210, 2005.
[98] A. Mazubert, D. F. Fletcher, M. Poux, and J. Aubin, “Hydrodynamics and mixing in continuous oscillatory flow reactors—Part I: Effect of baffle geometry,” *Chem. Eng. Process. Process Intensif.*, vol. 108, pp. 78–92, 2016.
[99] Z. Movasaghi, S. Rehman, and I. U. Rehman, “Fourier transform infrared (FTIR) spectroscopy of biological tissues,” *Appl. Spectrosc. Rev.*, vol. 43, no. 2, pp. 134–179, 2008.
[100] J. H. Kim, S. H. Kim, H. K. Kim, T. Akaike, and S. C. Kim, “Synthesis and characterization of hydroxyapatite crystals: A review study on the analytical methods,” *J. Biomed. Mater. Res.*, vol. 62, no. 4, pp. 600–612, 2002.
[101] A. Chauhan, M. K. Goyal, and P. Chauhan, “Powder XRD Technique and its Applications in Science and Technology,” *J. Anal. Bioanal. Tech.*, vol. 5, no. 6, pp. 1–5, 2014.
[102] F. Storti and F. Balsamo, “Particle size distributions by laser diffraction: sensitivity of granular matter strength to analytical operating procedures,” *Solid Earth*, vol. 1, pp. 25–48, 2010.
[103] P. Solutions, “SEM Analysis | SEM-EDS Analysis.” [Online]. Available: https://www.polymersolutions.com/capabilities/scanning-electron-microscopy-with-energy-dispersive-spectroscopy/. [Accessed: 16-Jan-2018].
[104] M. Asadabad and M. Eskandar, *Electron Diffraction Chapter*. Intech, 2016.
[105] N. D. Browning *et al.*, *Modeling Nanoscale Imaging in Electron Microscopy*. Springer Science+Business Media, 2012.
[106] “FLUIDINOVA.S.A.” [Online]. Available: http://www.fluidinova.com/. [Accessed: 26-Feb-1BC].
[107] F. Castro, A. Ferreira, F. Rocha, A. Vicente, and J. António Teixeira, “Characterization of intermediate stages in the precipitation of hydroxyapatite at 37ºC,” *Chem. Eng. Sci.*, vol. 77, no. 2, pp. 150–156, 2012.
[108] O. Mekmene, S. Quillard, T. Rouillon, and J. Bouler, “Effects of pH and Ca/P molar ratio on the quantity and crystalline structure of calcium phosphates obtained from aqueous solutions,” *Dairy Sci. Technol.*, vol. 89, no. 3–4, pp. 301–316, 2009.
[109] E. C. Moreno, R. T. Zahradnik, A. Glazman, and R. Hwu, “Precipitation of Hydroxyapatite From Dilute-Solutions Upon Seeding,” *Calcif. Tissue Res.*, vol. 24, no. 1, pp. 47–57, 1977.
[110] A. K. Lynn and W. Bonfield, “A novel method for the simultaneous, titrant-free control of pH and calcium phosphate mass yield,” *Acc. Chem. Res.*, vol. 38, no. 3, pp. 202–207, 2005.
[111] J. C. Heughebaert, S. J. Zawacki, and G. H. Nancollas, “The growth of nonstoichiometric apatite from aqueous solution at 37°C. I. Methology and growth at pH 7.4,” *J. Colloid Interface Sci.*, vol. 135, no. 1, pp. 20–32, 1990.
[112] J. P. Singh, N. P. Bansal, T. Goto, J. Lamon, S. R. Choi, and M. Mahmoud, *Processing and Properties of Advanced Ceramics and Composites IV*. The American Ceramic Society, 2012.
[113] M. H. Fathi, A. Hanifi, and V. Mortazavi, “Preparation and bioactivity evaluation of bone-like hydroxyapatite nanopowder,” *J. Mater. Process. Technol.*, vol. 202, no. 1–3, pp. 536–542, 2008.
[114] M. S. M. Arsad, P. M. Lee, and L. K. Hung, “Morphology and particle size analysis of hydroxyapatite micro- and nano-particles,” *CSSR 2010 - 2010 Int. Conf. Sci. Soc. Res.*, no. 3, pp. 1030–1034, 2010.
[115] M. Ansari, S. M. Naghib, F. Moztarzadeh, and A. Salati, “Synthesis and characterization of hydrxyapatite calcium hydroxide for dental composites.,” *Ceramics*, vol. 67, no. Figure 5, pp. 123–126, 2011.
[116] M. D. Castro and F. Priego-Capote, “Ultrasound-assisted crystallization (sonocrystallization),” *Ultrason. Sonochem.*, vol. 14, no. 6, pp. 717–724, 2007.
[117] H. Ishikawa, K. Hirabayashi, and T. Muramatsu, “The conformation of silk sericin,” *Sen’i*

Gakkaishi, vol. 28, no. 4–5. pp. 167–169, 1972.
[118] T. Matsumoto, M. Okazaki, M. Inoue, Y. Hamada, M. Taira, and J. Takahashi, "Crystallinity and solubility characteristics of hydroxyapatite adsorbed amino acid," *Biomaterials*, vol. 23, no. 10, pp. 2241–2247, 2002.
[119] M. Tavafoghi and M. Cerruti, "The role of amino acids in hydroxyapatite mineralization," *J. R. Soc. Interface*, vol. 13, no. 123, p. 20160462, 2016.
[120] S. Eiden, M. Viertelhaus, A. Heiß, K. A. Hoetzer, and J. Felsche, "The influence of amino acids on the biomineralization of hydroxyapatite in gelatin," *J. Inorg. Biochem.*, vol. 91, no. 3, pp. 481–486, 2002.
[121] D. Walsh, J. L. Kingston, B. R. Heywood, and S. Mann, "Influence of monosaccharides and related molecules on the morphology of hydroxyapatite," *J. Cryst. Growth*, vol. 133, no. 1–2, pp. 1–12, 1993.
[122] K. Ioku, S. Yamauchi, H. Fujimori, S. Goto, and M. Yoshimura, "Hydrothermal preparation of fibrous apatite and apatite sheet," *Solid State Ionics*, vol. 151, no. 1–4, pp. 147–150, 2002.
[123] H. bin Zhang, K. chao Zhou, Z. you Li, and S. ping Huang, "Plate-like hydroxyapatite nanoparticles synthesized by the hydrothermal method," *J. Phys. Chem. Solids*, vol. 70, no. 1, pp. 243–248, 2009.
[124] Z. Zhuang, H. Yamamoto, and M. Aizawa, "Synthesis of plate-shaped hydroxyapatite via an enzyme reaction of urea with urease and its characterization," *Powder Technol.*, vol. 222, pp. 193–200, 2012.
[125] A. K. Nayak, "Hydroxyapatite synthesis methodologies: An overview," *Int. J. ChemTech Res.*, vol. 2, no. 2, pp. 903–907, 2010.
[126] S. H. Maxian, J. P. Zawadsky, and M. G. Dunn, "Mechanical and histological evaluation of amorphous calcium phosphate and poorly crystallized hydroxyapatite coatings on titanium implants," *J. Biomed. Mater. Res.*, vol. 27, pp. 717–728, 1993.
[127] M. Yang *et al.*, "Biomimetic nucleation of hydroxyapatite crystals mediated by Antheraea pernyi silk sericin promotes osteogenic differentiation of human bone marrow derived mesenchymal stem cells," *Biomacromolecules*, vol. 15, no. 4, pp. 1185–1193, 2014.
[128] O. Suzuki, "Octacalcium phosphate: Osteoconductivity and crystal chemistry," *Acta Biomater.*, vol. 6, no. 9, pp. 3379–3387, 2010.
[129] Y. L. Renlong X. Ning W., "In situ TEM examinations of octacalcium phosphate tohydroxyapatite transformation," *Journal of Crystal Growth*, vol. 289. pp. 339–344, 2006.
[130] F. Barrere, P. Layrolle, C. Blitterswijk, and K. Groot, "Biomimetic coatings on titanium: a crystal growth study of octacalcium phosphate," *J. Mater. Sci. Mater. Med.*, vol. 12, no. 6, pp. 529–534, 2011.
[131] M. Das Murtey and P. Ramasamy, *Modern Electron Microscopy in Physical and Life Sciences*. Intech, 2016.
[132] W. Habraken, P. Habibovic, M. Epple, and M. Bohner, "Calcium phosphates in biomedical applications: Materials for the future?," *Mater. Today*, vol. 19, no. 2, pp. 69–87, 2016.
[133] Y. H. Terada S, Sasaki M, Yanagihara K, "Preparation of silk protein sericin as mitogenic factor for better mammalian cell culture," *US Natl. Libr. Med. Natl. Institutes Heal.*, vol. 100, no. 6, pp. 667–71, 2016.
[134] M. Vallet-Regí and J. M. González-Calbet, "Calcium phosphates as substitution of bone tissues," *Prog. Solid State Chem.*, vol. 32, no. 1–2, pp. 1–31, 2004.
[135] S. S. Jensen, M. M. Bornstein, M. Dard, D. D. Bosshardt, and D. Buser, "Comparative study of biphasic calcium phosphates with different HA/TCP ratios in mandibular bone defects. A long-term histomorphometric study in minipigs," *J. Biomed. Mater. Res. - Part B Appl. Biomater.*, vol. 90 B, no. 1, pp. 171–181, 2009.
[136] H. R. R. Ramay and M. Zhang, "Biphasic calcium phosphate nanocomposite porous scaffolds for load-bearing bone tissue engineering," *Biomaterials*, vol. 25, no. 21, pp. 5171–5180, 2004.
[137] H. Guo, J. Su, J. Wei, H. Kong, and C. Liu, "Biocompatibility and osteogenicity of degradable Ca-deficient hydroxyapatite scaffolds from calcium phosphate cement for bone tissue engineering," *Acta Biomater.*, vol. 5, no. 1, pp. 268–278, 2009.
[138] S. R. Paital and N. B. Dahotre, "Calcium phosphate coatings for bio-implant applications: Materials, performance factors, and methodologies," *Mater. Sci. Eng. R Reports*, vol. 66, no. 1–3, pp. 1–70, 2009.
[139] M. H. Prado Da Silva *et al.*, "Transformation of monetite to hydroxyapatite in bioactive coatings

on titanium," *Surf. Coatings Technol.*, vol. 137, no. 2–3, pp. 270–276, 2001.
[140] H. Yuan *et al.*, "Bone formation induced by calcium phosphate ceramics in soft tissue of dogs: a comparative study between porous alpha-TCP and beta-TCP," *J. Mater. Sci. Mater. Med.*, vol. 12, no. 1, pp. 7–13, 2001.
[141] D. Kovacevic, A. J. Fox, A. Bedi, and L. Ying, "Calcium-phosphate matrix with or without TGF-B3 improves tendon-bone healing after rotator cuff repair," *Am. J. Sports Med.*, vol. 39, no. 4, pp. 811–819, 2011.
[142] M. A. Khan, V. M. Wu, S. Ghosh, and V. Uskoković, "Gene delivery using calcium phosphate nanoparticles: Optimization of the transfection process and the effects of citrate and poly(l-lysine) as additives," *J. Colloid Interface Sci.*, vol. 471, no. 3, pp. 48–58, 2016.
[143] E. Verron, I. Khairoun, J. Guicheux, and J.-M. Bouler, "Calcium phosphate biomaterials as bone drug delivery systems: a review," *Drug Discov. Today*, vol. 15, no. 13–14, pp. 547–552, 2010.
[144] T. V Thamaraiselvi and S. Rajeswari, "Biological Evaluation of Bioceramic Materials - A Review," *Trends Biomater. Artif. Organs*, vol. 18, no. 1, pp. 9–17, 2004.
[145] R. F. Bonan, P. R. F. Bonan, A. U. D. Batista, J. E. Oliveira, R. R. Menezes, and E. S. Medeiros, "Métodos de reforço microestrutural da hidroxiapatita," *Cerâmica*, vol. 60, pp. 402–410, 2014.
[146] S. Pramanik, A. K. Agarwal, K. N. Rai, and A. Garg, "Development of high strength hydroxyapatite by solid-state-sintering process," *Ceram. Int.*, vol. 33, no. 3, pp. 419–426, 2007.
[147] B. Nasiri-Tabrizi, P. Honarmandi, R. Ebrahimi-Kahrizsangi, and P. Honarmandi, "Synthesis of nanosize single-crystal hydroxyapatite via mechanochemical method," *Mater. Lett.*, vol. 63, no. 5, pp. 543–546, 2009.
[148] Y. Cai, D. Mei, T. Jiang, and J. Yao, "Synthesis of oriented hydroxyapatite crystals: Effect of reaction conditions in the presence or absence of silk sericin," *Mater. Lett.*, vol. 64, no. 24, pp. 2676–2678, 2010.
[149] J. Liu, Y. Liu, Y. Kong, J. Yao, and Y. Cai, "Formation of vaterite regulated by silk sericin and its transformation towards hydroxyapatite microsphere," *Mater. Lett.*, vol. 110, pp. 221–224, 2013.
[150] K. Sakamoto and J. C. Elliott, "Shape-controlled synthesis of hydroxyapatite from α-tricalcium bis (orthophosphate) in organic-aqueous binary systems," *Nippon Kagaku Kaishi*, vol. 7, pp. 1033–1041, 2002.
[151] G. Zhang, J. Chen, S. Yang, Q. Yu, Z. Wang, and Q. Zhang, "Preparation of amino-acid-regulated hydroxyapatite particles by hydrothermal method," *Mater. Lett.*, vol. 65, no. 3, pp. 572–574, 2011.
[152] S. Bose and S. K. Saha, "Synthesis and Characterization of Hydroxyapatite Nanopowders by Emulsion Technique," *Chem. Mater.*, vol. 15, no. 23, pp. 4464–4469, 2003.
[153] A. B. Hazar Yoruç and Y. Ipek, "Sonochemical synthesis of hydroxyapatite nanoparticles with different precursor reagents," *Acta Phys. Pol. A*, vol. 121, no. 1, pp. 230–232, 2012.
[154] S. K. Ghosh, S. K. Roy, B. Kundu, S. Datta, and D. Basu, "Synthesis of nano-sized hydroxyapatite powders through solution combustion route under different reaction conditions," *Mater. Sci. Eng. B Solid-State Mater. Adv. Technol.*, vol. 176, no. 1, pp. 14–21, 2011.
[155] J. S. Cho and Y. C. Kang, "Nano-sized hydroxyapatite powders prepared by flame spray pyrolysis," *J. Alloys Compd.*, vol. 464, no. 1–2, pp. 282–287, 2008.
[156] H. Yun *et al.*, "Extraction conditions of Antheraea mylitta sericin with high yields and minimum molecular weight degradation," *Int. J. Biol. Macromol.*, vol. 52, no. 1, pp. 59–65, 2013.
[157] G. Freddi, R. Mossotti, and R. Innocenti, "Degumming of silk fabric with several proteases," *J. Biotechnol.*, vol. 106, no. 1, pp. 101–112, 2003.
[158] N. M. Mahmoodi, M. Arami, F. Mazaheri, and S. Rahimi, "Degradation of sericin (degumming) of Persian silk by ultrasound and enzymes as a cleaner and environmentally friendly process," *J. Clean. Prod.*, vol. 18, no. 2, pp. 146–151, 2010.
[159] P. Aramwit, T. Siritientong, and T. Srichana, "Potential applications of silk sericin, a natural protein from textile industry by-products," *Waste Manag. Res.*, vol. 30, no. 3, pp. 217–224, 2012.
[160] M. Sasaki, H. Yamada, and N. Kato, "A Resistant Protein, Sericin Improves Atropine-Induced Constipation in Rats," *Food Sci. Technol. Res.*, vol. 6, no. 4, pp. 280–283, 2000.
[161] A. R. Lalit Jajpura, "The Biopolymer Sericin: Extraction and Applications," *J. Text. Sci. Eng.*, vol. 5, no. 1, pp. 1–5, 2015.
[162] "Pure Sericin." [Online]. Available: https://www.puresericin.com/en/healthcare/#chounai. [Accessed: 22-Dec-2017].

[163] “Silk Sericin Powder.” [Online]. Available: https://www.alibaba.com/product-detail/Best-quality-pure-cosmetic-grade-Silk_60645158751.html?spm=a2700.7724857.main07.28.567e3782kS2oCg&s=p. [Accessed: 22-Dec-2017].
[164] “Sericin+.” [Online]. Available: https://www.sericinplus.com/. [Accessed: 22-Dec-2017].
[165] “KRUUSE Silk suture.” [Online]. Available: https://www.kruuse.com/en/ecom/Suturer_og_nåle/Peelpack_non_resorb/SILK_skær_nål/prod_152380.aspx. [Accessed: 22-Dec-2017].
[166] “SERI® Surgical Scaffold.” [Online]. Available: https://www.seri.com/product/biocompatibility.html. [Accessed: 22-Dec-2017].

Appendices

A.1 - Characteristics of interest in a biomaterial [1].

Characteristics	
Biocompatibility	Porosity
Physical properties (structure, morphology and size)	Degradation
Chemical composition	Resistance to corrosion
Surface Topography	Mechanical resistance

A.2 - Biomedical materials with CaPs [3].

Biomaterial	Reference
Bone fillers	[134],[135]
Bone tissue engineering scaffolds	[136],[137]
Bioactive coatings	[138],[139]
Soft tissue repairs	[140],[141]
Drug/ protein/gene loading and delivery systems	[142],[143]

A.3 - Types of bioceramics used in biomedical engineering [144].

Material	Classification
Alumina (Al_2O_3); Zirconia (ZrO_2); Carbon	Bioinert
Bioglass and glass ceramics	Bioactive
CaPs (HAp and ß-tricalcium phosphate)	Bioactive and biodegradable

B.1 - Ca/P of different CaPs [145],[132].

CaPs	Standard abbreviation	Chemical formula	Ca/P	Occurrence
Hydroxyapatite	HAp	$Ca_{10}(PO_4)_6(OH)_2$	1,67	Enamel, dentin, bone, dental and urinary calculus, stones, soft tissue calcification
Amorphous calcium phosphate	ACP	$Ca_xH_y(PO_4)_z.nH_2O$	1,5 (1,20-2,20)	Amorphous urinary and dental calculus
Tricalcium phosphate	(α, α´, ß, ϒ) TCP	$Ca_3(PO_4)_2$	1,5	Dental and urinary calculi, salivary stones, dental caries, soft tissue calcification
Octacalcium phosphate	OCP	$Ca_8H_2(PO_4)_6.{}_5H_2O$	1,33	Amorphous urinary and dental calculus
Dicalcium phosphate dehydrate	DCPD	$CaHPO_4.2H_2O$	1,0	Dental calculus, decomposed bones
Dicalcium phosphate dehydrate	DCP	$CaHPO_4$	1,0	-
Calcium pyrophosphate	CPP	$Ca_2P_2O_7$	1,0	-
Calcium pyrophosphate dihydrate	CPPD	$Ca_2P_2O_7.2H_2O$	1,0	Deposits of pseudo-drops in fluids
Calcium heptaphosphate	HCP	$Ca_7(P_5O_{16})_2$	0,7	-
Monocalcium phosphate monohydrate	MCPM	$Ca_7\ (H_2PO_4)_2.H_{20}$	0,5	-

B.2 - Methods for the synthesis of HAp.

Methods		Characterization		Ref.
		Method	Particles	
Dry methods	Solid-state	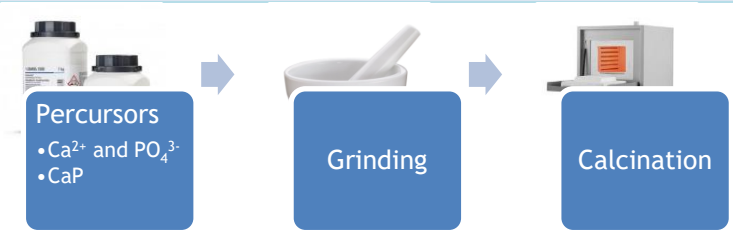	-Heterogeneous and irregular; -High crystallinity; Size: micron; Shapes described in the literature: variable (irregular/formless, sphere).	[146]
	Mechanochemical	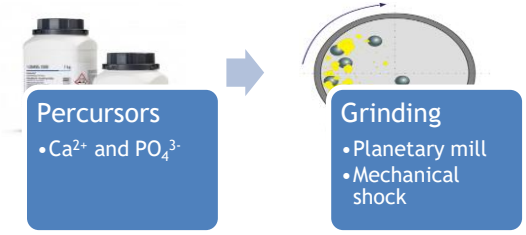	-Well-defined structure, in comparison with de solid-state method; -Non-stoichiometric; -High crystallinity; Size: nano; Shapes described in the literature: variable (irregular/formless, sphere, rod, needle).	[147]
Wet methods	**Chemical precipitation**	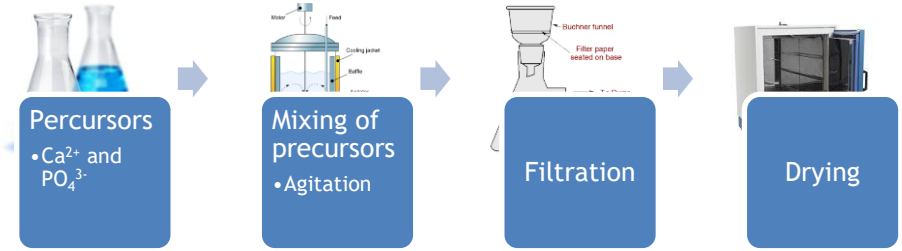	-Non-stoichiometric; -Low crystallinity; -Formation of agglomerates; Size: nano; Shapes described in the literature: variable (irregular/formless, sphere, rod, needle, plate, sheet, leaf, enamel prism-like structures).	[107], [148], [149]

	Hydrolysis	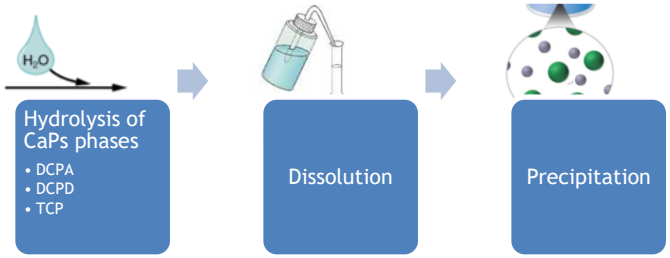	-High cost; -Stoichiometric; Size: variable; Shapes described in the literature: variable (irregular/formless, rod, needle, leaf, enamel prism-like structures).	[150]
	Sol-gel	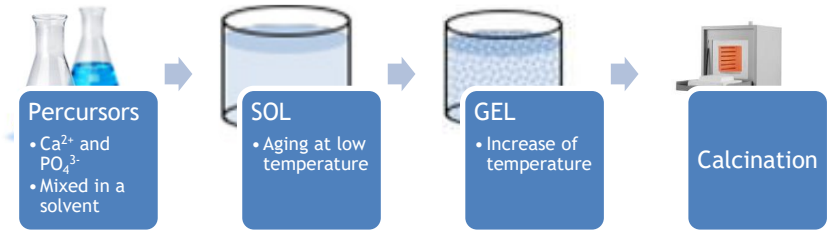	-Stoichiometric; Size: nano; Shapes described in the literature: variable (irregular/formless, sphere, rod, needle).	[125]
	Hydrothermal	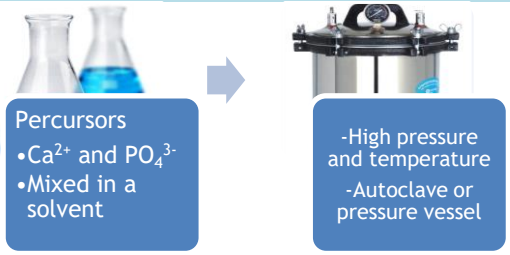	-Stoichiometric; -High cost; -High crystallinity; Size: nano or micron; Shapes described in the literature: variable (irregular/formless, sphere, rod, needle).	[151]

	Emulsion / Micro-emulsion	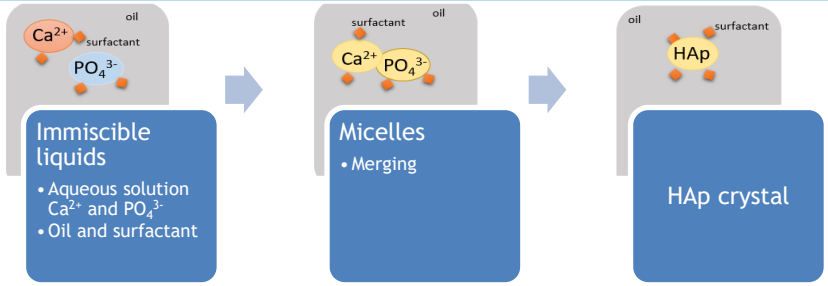	-High cost; -Low crystallinity; -Non-stoichiometric; Size: nano; Shapes described in the literature: variable (irregular/formless, sphere, rod, needle, self-assembled nanorods).	[152]
	Sonochemical	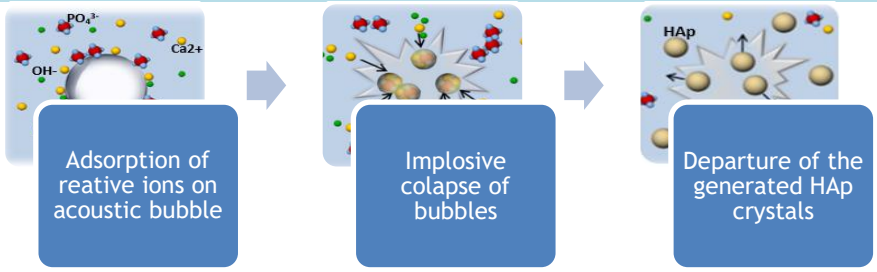	-Low agglomeration degree; Size: nano; Shapes described in the literature: variable (irregular/formless, sphere, rod, needle).	[153]
High-temperature processes;	Combustion	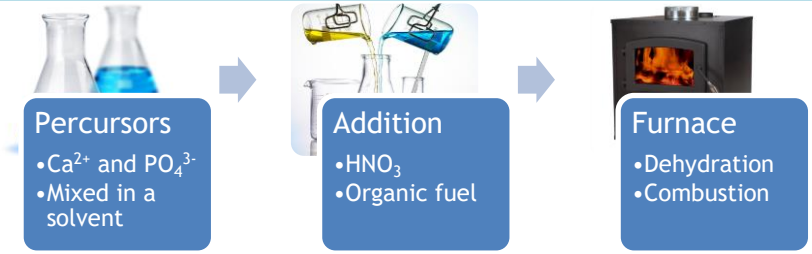	-High crystallinity; Size: nano; Shapes described in the literature: variable (irregular/formless, sphere, rod, needle).	[154]
	Pyrolysis (spray pyrolysis)	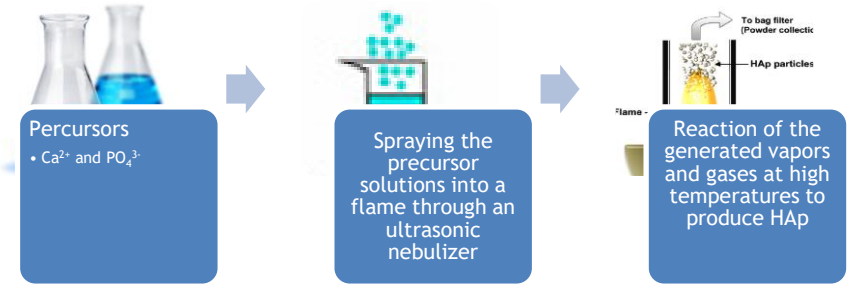	-Stoichiometric; -High crystallinity; Size: nano; Shapes described in the literature: variable (irregular/formless, sphere, rod, needle).	[155]

C.1 - Degumming methods to extract raw silk proteins.

Degumming method			Advantages	Disadvantages	Ref.
Chemical treatment	Soap-alkaline	-Solution of Sodium carbonate and Marseille soap;	-Suitable for obtaining clean and isolated fibroin; -Complete removal of SS from the cocoons.	-Difficult to recover and separate SS from the soap; -Promotes the hydrolysis of the SS chain structure, losing some functional properties; -Marseille soap is expensive.	[57], [15], [156]
	Alkane or acid solutions	-Sodium carbonate, urea, and urea-mercaptoethanol or sodium chloride;	-High efficiency; -Cheaper.	-Purification steps are necessary to remove impurities (dialysis).	[57], [156]
Enzimatic	Alkaline, acid or Neutral proteases	-Alkylase, alkaline protease.	-Effective; -No contaminants.	-Expensive process; -Limited applications (promotes the specific proteolytic hydrolysis of the primary SS chain structure, which causes a molecular weight reduction).	[60], [156], [157], [158]
Boiling in water	By heat or heat under pressure	-Water.	-Does not introduce impurities and byproducts; -Does not require chemicals; -Simple procedure; -No purification steps needed.	-Procedure is too long; -Causes fibroin damage.	[60], [61], [63], [156], [159]

C.2 - SS Applications.

Industry	Applications	Properties	Products and Companies	Ref.
Food	-Food coating; -Dietary additive.	-Digestible; -Combat constipation; -Biocompatibility; -Antioxidant; -Tyrosine kinase inhibitor.	-Pure Sericin: powder.	[56],[59], [60],[160], [161],[162], [64]
Cosmetic Products	-Solar Protectors; -Skin elasticity creams; -Moisturizing and anti-aging creams; -Nail and hair cosmetics.	-Resistance to UV rays; -Moisturizing; -Biocompatibility and biodegradability; -Skin adhesion; -Strong affinity to keratin; -Elasticity.	-Sericin +: several body creams; -Xi'an Prius biological Engineering: facial powder.	[56],[161], [163],[164]
Biomedical Engineering	- Biomaterials (membranes, hydrogels, scaffolds) for skin regeneration / wound treatment.	-Absorb excess exudates and keeps a moist environment; -Biocompatibility; -Stimulating cell growth -Antibacterial properties; -Skin adhesion; -Anticoagulant; -Crosslinking.	-Kruuse: silk suture; -SERI: Surgical Scaffold.	[56],[59], [60],[63], [159],[165], [166]

D - Published papers on HAp/SS materials.

Ref.	Topic		Methodology	Product characteristics and observations	Application
[6]	- Mechanism of mineralization in biological systems (structural effect of SS on HAp nucleation).	HAp/SS films.	- Films were prepared from different SS solutions and cast into a polyethylene film. The cast films were exposed to the SBF (Simulated body fluid), which is a metastable CaP solution with inorganic ion concentrations almost equal to those in human blood plasma; - SS extraction in boiling water.	- Films with different proportions of SS in β-sheet structure were obtained. Deposition of HAp occurred in the sample with the highest content of β-sheet; - Heterogeneous nucleation of HAp depends on the carboxyl group content and its arrangement of. SS has a high number of carboxyl groups on its structure. When SS adopts an ideal β-sheet structure, 10% of the carboxyl groups can be arranged perpendicular to the sheet which facilitates interaction with the surrounding environment.	- Understanding the mechanism of mineralization in biological systems; - Design of novel organic polymers for the preparation of structures similar to the mineral bone.
[40]	- Cell attachment and proliferation (Investigate the effect of SS application over HAp surface on osteoblast cells proliferation).		- HA films with SS on the surface were sintered; - Different concentration of SS were used; - Hydrothermal method for the synthesis of HAp/SS; - SS extraction by chemical treatment; - The other reagents used were $CaSO_4.2H_2O$ and $(NH_4)_2HPO_4$.	- SS application over HAp surface increased the amount of osteoblast cells proliferation; - SS concentration did not influence cells proliferation;	- Bone tissue engineering.
[4]	- Role of organic matrix in biomineralization.		- HAp/SS composite films were obtained by mineralizing a flexible ethanol-treated SS film in SBF; - SS extraction in boiling water.	- HAp deposited in the film is a OHAp, with poor crystallinity and a c-axis direction growth similar to natural bone mineral. - HAp/SS film showed excellent cell viability resulting from the deposition of HAp and its 3D structure.	- Bone tissue engineering.

[148]	- Understanding of the process of Biomineralization (Effect of reaction conditions in the presence or absence SS).	HAp/SS nano compo-sites.	- SS was used to modulate the assembly of nanosized HAp crystals; - Wet precipitation method for the synthesis of HAp/SS crystals; - Different concentration of SS and mineralization times were used; - The other reagents used were NaOH, $CaCl_2$ and Na_2HPO_4; - The reactor used was a ST.	- It was found that a homogeneous assembly could be obtained in the presence of SS, which held a highly ordered microstructure and poor crystallinity; - In the absence of SS, an oriented aggregate could also be prepared at 50°C and pH 10.	- Understanding the mechanism of mineralization in biological systems; - Biomedical applications and fundamental studies of cell-matrix interactions.
[66]	- Role of organic matrix in biomineralization (Effect of SS concentration and mineralization time on the formation HAp).		- Same chemical methodology as the previous paper ([66]).	- HAp nanocrystals similar to the natural enamel were obtained; - Preferential growth of HAp along c-axis with the increase of SS concentration; - Higher concentration of SS and longer mineralization time was in favor of larger crystal formation; - The biocompatibility of the assemblies was evaluated *in vitro* and showed to promote cell differentiation and proliferation.	- Biomedical applications for bone tissue and fundamental studies of cell-matrix interactions.
[127]	- Biomimetic mineralization of HAp mediated by SS.		- Wet precipitation method; - SS extraction in boiling water. - The other reagents used were $CaCl_2$, Na_2HPO_4, $NaHCO_3$. - The reactor used was a ST.	- Nucleation of HAps in the form of nanoneedles while self assembling into ß-sheet conformation; - HAp/SS promotes osteogenic differentiation of human BMSCs (Bone marrow mesenchymal stem cells).	- Potential scaffold for tissue engineering.

E - pH value and duration of the phases identified for the experimental conditions studied in the ST.

		Different stages					
Experimental condition	**Monitored variables**	**1**	**2**	**3**	**4**	**5**	**6**
HAp	**Δt (s)**	2	7	2	90	110	*
	ΔpH	8,00-7,40	7,40-7,25	7,25-6,70	6,70-6,50	6,50-6,00	6,00-5,60
HAp/SS1	**Δt (s)**	9	10	10	70	80	*
	ΔpH	8,85-7,50	7,50-7,25	7,25-6,50	6,50-6,45	6,45-5,85	≈5,85-5,50
HAp/SS2	**Δt (s)**	12	62	15	80	110	*
	ΔpH	8,55-7,40	7,40-7,30	7,30-6,65	6,65-6,45	6,45-6,00	6,00-5,70

*until the end of the experiment

F - Experiment performed with 10 times the initial reactants concentration (A) FTIR (B) SEM and (C) TEM.

The particles obtained with this experiment in the meso-OFR were analyzed by FTIR (A), SEM (B), and TEM analysis (C), where electron diffraction pattern was also performed. Through FTIR, it is possible to verify that the sample obtained presents only two characteristic HAp bands at 1026 cm^{-1} and at 557 cm^{-1}, attributed to PO_4^3. These bands have lower intensity when compared to commercial HAp. Through SEM and TEM, it is verified that the particles are in the µm order, presenting a rectangular-like morphology. The electron diffraction patterns showed a sharp and bright central ring, surrounded by smaller bright spots, which is characteristic of a polycrystalline material. When compared to the other particles obtained, these particles present higher crystallinity, larger size and a different morphology. Results suggest thus that the sample obtained is not single-phased HAp, but a mixture of nano-HAp and what appears to be another CaP.